GEOPHYSICAL PROSPECTING USING SONICS AND ULTRASONICS

Geophysical prospecting refers to measurements and interpretations of data to infer subsurface compositions of earth at various depths. These measurements may be based on electrical, nuclear, and acoustic techniques depending on the physical or chemical properties of the subsurface formation that are to be determined. This article focuses on applications of acoustic techniques that are used in the exploration and production of hydrocarbons from underground reservoirs.

Hydrocarbons are found in porous rocks. The intergranular nature of these rocks is inferred from their volume fraction of pores, referred to as porosity, and their connectivity, referred to as permeability. The pores of a rock may be filled with brine or hydrocarbons. The partition between these two phases is described in terms of saturation. It is also of interest to distinguish between the liquid and gas phases of hydrocarbons found in porous rocks. To aid in the design of the production phase of oil and gas wells, it is also of interest to determine the pressure and temperature of the fluid in the pores. In summary, the quantities of primary interest in the design and development of oil and gas reservoirs are (1) porosity, (2) saturation, (3) permeability, (4) pressure, and (5) temperature of pore fluid; interested readers may refer to Refs. 1 and 2.

Following an identification of promising geological areas by means of surface seismic surveys, a borehole is drilled to locate depths of potential hydrocarbon reservoirs. Figure 1(a) shows a schematic of a borehole together with the surface equipment and a sonde that carries various types of sources and receivers for downhole measurements. A borehole fluid, also referred to as mud, is used to facilitate the drilling and prevent the well from collapsing under the pressure exerted by the surrounding formation. These wells may range from 1000 to 10,000 m in depth. The environment in these wells can have temperatures exceeding 175°C and pressures up to 138 MPa (20,000 psi). Periodically, drilling is interrupted to evaluate the presence of hydrocarbons over a certain depth range in the well by means of open-hole measurements, also known as wireline logging operations. Open-hole sonic measurements are typically made at frequencies ranging from 0.5 kHz to 20 kHz. However, open-hole imaging of sedimentary layers and borehole cross-sectional shape requires frequencies ranging from 200 kHz to 600 kHz.

If open-hole acoustic, electrical, and nuclear measurements confirm the presence of a hydrocarbon reservoir, a heavy steel casing is lowered into the well and cemented into the borehole to prepare the well for production as shown in Fig. 1(b). The cemented casing keeps the hole from collapsing and isolates hydrocarbon-bearing zones from water-bearing ones. Finally, the casing and cement are perforated to allow the oil and gas to flow into the well for production. Cased-hole ultrasonic measurements are typically made at frequencies ranging from 100 kHz to 2.5 MHz.

This article contains two major sections covering measurements introduced above: “Sonic Measurements” and “Ultrasonic Measurements.”

SONIC MEASUREMENTS

Sonic measurements play an important role in estimating the mechanical attributes of rocks that are crucial in an efficient and safe production and development of oil and gas wells. For instance, the granular rock may be consolidated or unconsolidated. This mechanical attribute of the rock impacts analyses of wellbore stability as well as sanding in a producing well. Sanding refers to the mechanical failure of the formation in

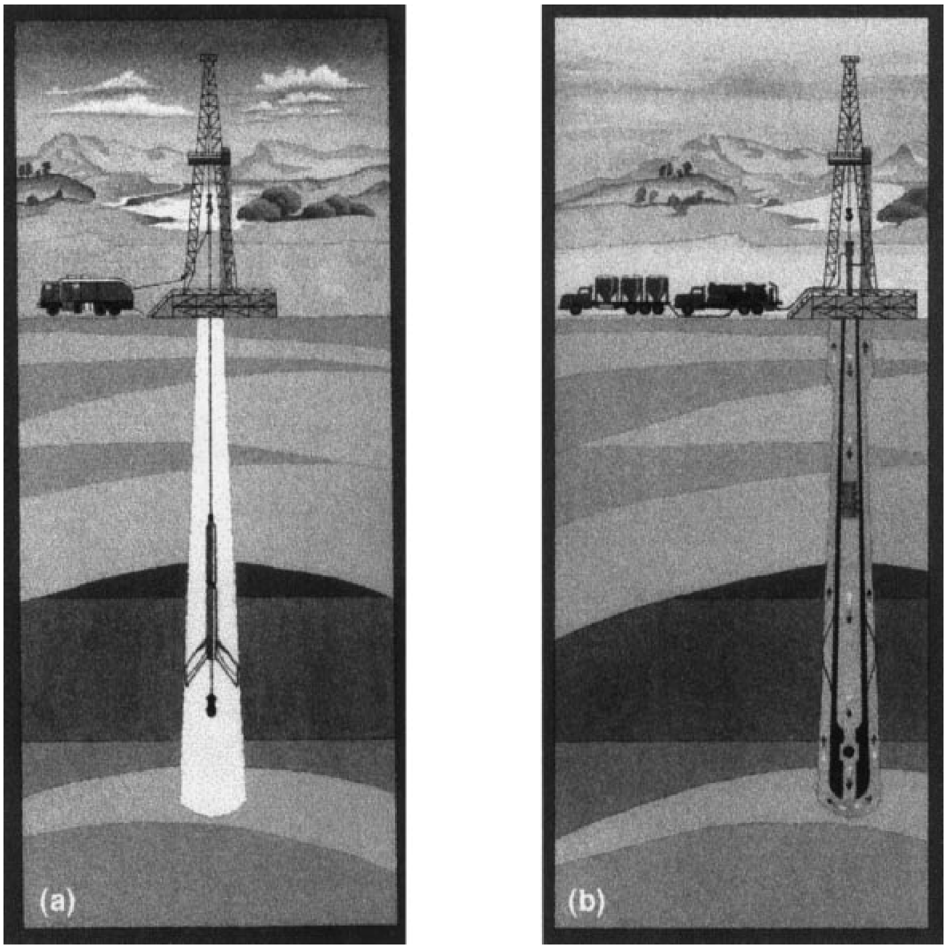

Figure 1. (a) Open-hole measurements. A wireline tool in an open hole measures formation properties to determine the depth and producibility of hydrocarbon reservoirs. (b) Casing and cementing of a well. Completion of a well for production involves lowering a steel casing and pumping cement through the casing to bond it to the surrounding formation. Cased-hole measurements are conducted in preparation for production. (After Ref. 58, with permission.)

the borehole vicinity that results in sand particles mixed with liquid hydrocarbon flowing into a producing well. This attribute can be estimated from the formation lithology together with the ratio of compressional and shear wave velocities that is related to the Poisson's ratio of the formation. Another application of acoustic measurements in a borehole is in the identification of homogeneous versus fractured rocks. The existence of natural or induced fractured rocks significantly alters the formation permeability that directly contributes to the efficiency of production. Aligned fractures in rocks produce fractured–induced shear anisotropy that can be measured by a borehole flexural logging probe. Other applications of acoustic measurements in rocks include: estimation of rock porosity; identification of oil- versus gas-filled porous formations; identification of near-wellbore invasion of mud fluid in a porous formation; overpressured regions of the formation; and the presence of large tectonic stresses that can produce radial alteration in the borehole vicinity.

Acoustic measurements can yield elastic parameters of the propagating medium. These measurements are generally based on (1) interval transit time or velocity of nondispersive plane waves and dispersive guided waves, (2) amplitude attenuation, and (3) reflection amplitude estimates from a stratified formation. Most of the acoustic measurements in geophysical prospecting are based on travel time measurement of compressional and shear plane waves in a homogeneous formation. If the propagating medium consists of both solid and fluid phases, it has been found that the total time delay Δt can be expressed in terms of delays in the two phases given by the following expression (1,2):

$$\Delta t = \Delta t_{\text{solid}}(1-\phi) + \Delta t_{\text{fluid}}\phi \tag{1}$$

which is known as the Wyllie time-average equation (3). This equation provides a linear relationship between the interval transit time and the rock porosity ϕ. Equation (1) can also be expressed in terms of average compressional wave velocity V and those in the solid V_{solid} and fluid V_{fluid} portions of the composite.

$$\frac{1}{V} = \frac{(1-\phi)}{V_{\text{solid}}} + \frac{\phi}{V_{\text{fluid}}} \tag{2}$$

This rudimentary interpretation of acoustic measurement in a borehole marks the beginning of an increase in the role of sonic measurements in geophysical prospecting. In addition to the measurements of compressional and shear wave velocities in homogeneous formations, recent developments include measurements of radial and azimuthal variation of such plane wave velocities in homogeneous and anisotropic formations.

Compressional headwaves are generally the first arrivals from the formation. These arrivals are accentuated by the presence of borehole resonances that occur for wavelengths in the borehole fluid comparable to the borehole diameter. Multiples of headwave resonances will be generated with a sufficiently large bandwidth transmitter (4). In soft formations, these borehole resonances occur at the cutoff frequencies of leaky compressional modes. These modes are both dispersive and attenuative. The velocity of these modes asymptotically approaches the borehole fluid velocity at high frequencies (5).

Radial variation of compressional velocity can be estimated by a tomographic reconstruction of refracted headwave measurements with short and long transmitter–receiver spacings (6).

Radial variation of shear velocity can be estimated by measuring borehole flexural dispersion over a reasonably wide bandwidth. Radial variations of compressional and shear wave velocities are indicators of alteration in the vicinity of a borehole that can be caused by borehole stress concentrations, mechanical damage, and shale swelling. Such variations in plane wave velocities also cause perturbations in the borehole-guided mode dispersions from the case of homogeneous formations. In particular, changes in borehole flexural dispersions caused by alterations can be inverted to estimate radial variation of shear velocity in slow formations. While the mechanical state of rock in the borehole vicinity is of interest in analyzing formation competency for perforations and prediction of potential sanding, formation compressional and shear velocities in the far-field are the ones that are needed for petrophysical and geophysical applications. These applications may include lithology identification, porosity estimation, synthetic seismograms, and calibration of inputs to amplitude variation with offset (AVO) analysis.

Rock porosity is estimated from compressional velocity measurements and formation lithology by correlating the ratio of compressional to shear velocities (V_P/V_S) with porosity (or Δt_c). In clastic rocks, a lower ratio of (V_P/V_S) for a given shear slowness defined simply as the inverse of shear velocity has been found to correlate well with the hydrocarbon-bearing sandstones as described by Williams (7). This correlation is sometimes used to differentiate hydrocarbon-bearing sandstones from water-bearing sandstones and shales in the absence of other measurement indicators. It is a particularly useful technique in zones with fresh formation water where high resistivities are common in water-bearing intervals and the distinction between high-resistivity oil and low-resistivity brine cannot be made.

Newer applications of sonic measurements are in estimating formation anisotropy. Formation anisotropy may be caused by (a) intrinsic microlayerings, such as in shales, (b) aligned fractures, (c) thin beddings, and (d) any tectonic stresses transverse to the propagation direction. Anisotropy caused by the first three sources are described by linear anisotropic elasticity where the material may exhibit various symmetries with respect to the borehole measurement axes. The measurement axes coincide with the borehole axis and two orthogonal axes in the azimuthal plane. The lowest material symmetry is that of triclinic materials. However, wave propagation in the presence of prestress must be described by equations of motion for small dynamic fields superposed on a static bias that are derived from a nonlinear formulation.

It is also of importance to distinguish between stress-induced and other sources of shear anisotropy. Recently, it has been found that a horizontal uniaxial stress in the formation causes a crossover in flexural dispersions in a vertical borehole for the radial polarization aligned parallel and perpendicular to the stress direction. This crossover in flexural dispersions is caused by stress-induced radial heterogeneities in acoustic wave velocities that are different in the two principal stress directions. Other sources of borehole flexural anisotropy caused by finely layered dipping beds, aligned fractures, or microstructures found in shales exhibit neither such radial heterogeneities nor flexural dispersion crossover. Consequently, a crossover in flexural dispersion can be used as an indicator of stress-induced anisotropy. In the presence of stress-induced shear anisotropy, the fast shear direction coincides with the maximum stress direction in the far-field, and the magnitude of shear anisotropy is proportional to the product of stress magnitude and formation nonlinear constant. Additional measurements of borehole guided modes, such as axisymmetric Stoneley and flexural dispersions, at two borehole pressures yield the two formation nonlinear constants that can be used to estimate the magnitude of stress from the measured azimuthal shear anisotropy.

When the shear anisotropy is caused by aligned fractures, the fast shear direction coincides with the fracture strike, and the magnitude of shear anisotropy is related to the fracture density and fracture compliance.

ELASTIC WAVE PROPAGATION IN A BOREHOLE

An acoustic source in a fluid-filled borehole generates head waves as well as relatively stronger borehole-guided modes. Figure 1 shows a schematic diagram of a fluid-filled borehole in a formation. A standard sonic measurement system consists of placing a piezoelectric source and an array of hydrophone receivers on the borehole axis. The piezoelectric source is configured in the form of either a monopole source or a dipole source. The source bandwidth typically ranges from 0.5 kHz to 20 kHz. A monopole source generates primarily an axisymmetric family of modes together with compressional and shear headwaves. In contrast, a dipole source primarily excites the flexural family of borehole modes together with compressional and shear headwaves. The headwaves are caused by coupling to plane waves in the formation that propagate along the borehole axis. An incident compressional wave in the borehole fluid produces critically refracted compressional waves in the formation. These refracted waves traveling along the borehole surface are also known as compressional head waves. The critical incidence angle, θ_i, equals $\sin^{-1}(V_f/V_c)$, where V_f is the compressional wave speed in the borehole fluid and where V_c is the compressional wave speed in the formation. As the compressional head wave travels along the interface, it radiates energy back into the fluid that can be detected by hydrophone receivers placed in the fluid-filled borehole. In fast formations, shear head waves can be similarly excited by a compressional wave at the critical incidence angle $\theta_i = \sin^{-1}(V_f/V_s)$, where V_s is the shear wave speed in the formation. It is also worth noting that head waves are excited only when the wavelength of the incident wave is significantly smaller than the borehole radius so that the boundary can be effectively treated as a planar interface. In a homogeneous and isotropic model of fast formations, compressional and shear head waves can be generated by a monopole source placed in a fluid-filled borehole for determining the formation compressional and shear wave speeds.

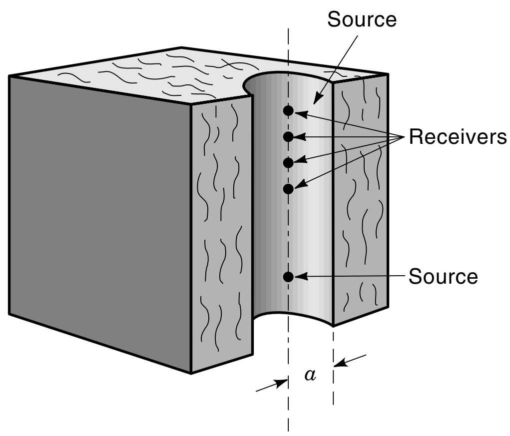

Figure 2. A fluid-filled borehole with a source and an array of receivers.

Figure 2 illustrates how a monopole source placed in a liquid-filled borehole excites compressional and shear headwaves followed by relatively higher amplitude Stoneley wave in a hard (fast) formation. A fast or slow formation implies that the formation shear wave velocity is higher or lower than the borehole-fluid compressional velocity, respectively. Figure 3 displays compressional headwaves followed by relatively higher amplitude flexural wave caused by a dipole source in a soft (slow) formation. Note that shear headwaves are not detected by hydrophones placed in the borehole fluid in the case of slow formations. These waveforms are processed by a standard slowness-time coherence (STC) algorithm to extract the compressional and shear slownesses by an appropriate windowing of the recorded waveforms (8). Slowness is the reciprocal of velocity and is typically expressed as the interval time per unit distance of travel by the elastic wave in standard sonic tools. A standard unit for slowness is μs/ft (μs/ft = 0.3048 μs/m). Figure 4 shows a typical array of recorded time waveforms together with time varying windows used in the STC processing. The STC-algorithm operates on a set of time windows applied to the recorded waveforms. The window position is determined by an assumed arrival time at the first receiver and an assumed slowness. A scalar semblance is computed for the windowed waveform segments. Local maxima of the semblance function are identified by a peak-finding algorithm and the corresponding slowness value is associated with a particular arrival in the wavetrain. The semblance is a measure of the presence or absence of an arrival with a given slowness and arrival time and its value lies between 0 and 1. If the assumed slowness and arrival time do not coincide with that of an actual arrival, the semblance takes on a smaller value. Figure 5 shows typical results from the STC processing on two different frequency bands. Comparing the low-frequency window (0.5 kHz to 1.5 kHz) with the high-frequency window (1 kHz to 2 kHz), we note that the high-frequency window exhibits two distinct peaks. The lower peak represents the faster velocity in the undisturbed region which coincides with the low-frequency window peak slowness. The slower arrival in the high-frequency window denotes the formation slowness in the altered zone. Therefore, the low-frequency window exhibits a distinct high-quality peak essentially unaffected by the altered zone. The semblance contour plot is typically mapped into a compressional

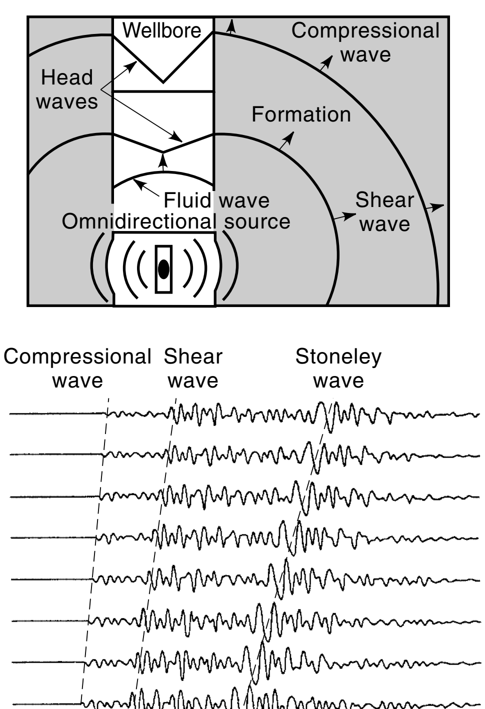

Figure 3. Elastic wave propagation in a hard (fast) formation caused by a monopole source (top); typical sonic waveforms recorded by a monopole tool in a fast formation (bottom).

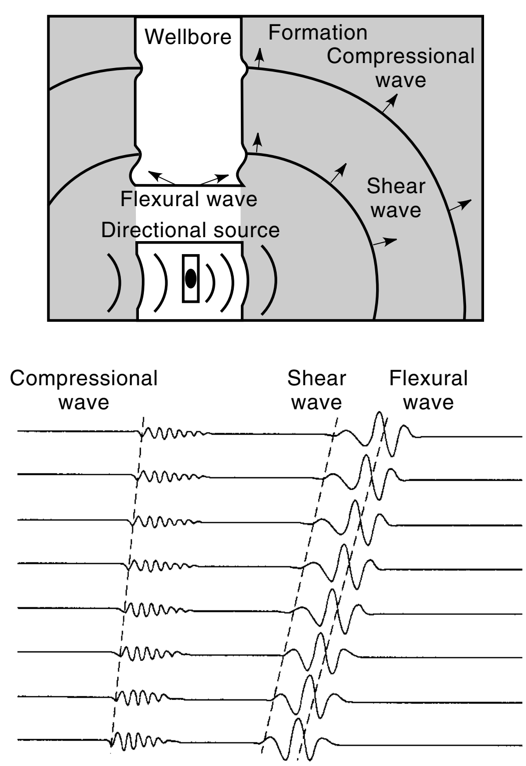

Figure 4. Elastic wave propagation in a soft (slow) formation caused by a dipole source (top); typical dipole sonic waveforms recorded in a slow formation (bottom).

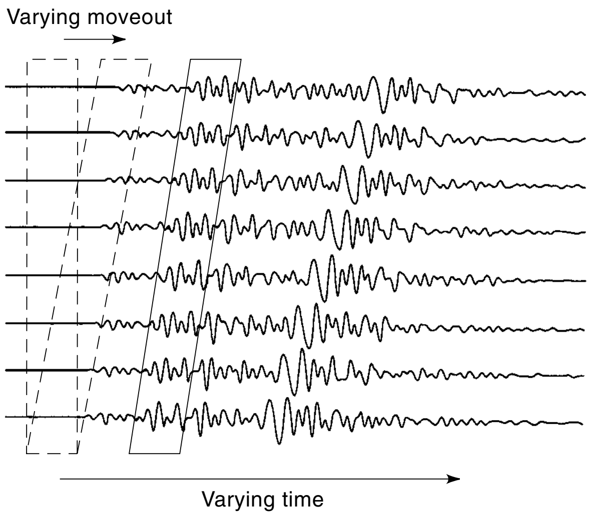

Figure 5. STC processing with different processing windows.

and shear slowness log that shows the formation compressional and shear slownesses as a function of depth as shown in Fig. 6.

Two standard interpretations of these sonic logs are illustrated in Figs. 7 and 8. Figure 7 shows an example of how V_P/V_S versus Δt_c for the compressional wave expressed in μs/ft illustrates lithology trends with respect to porosity that is proportional to Δt_c. The V_P/V_S ratio is also related to the Poisson's ratio of the material as shown in Fig. 9. This relationship helps in the identification of different lithologies.

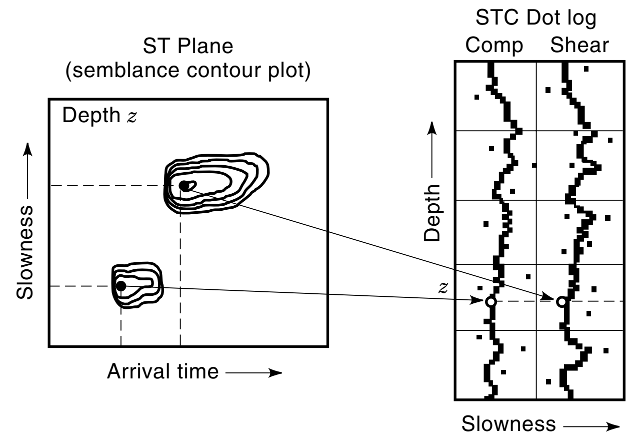

Figure 7. STC contour plot mapped into a sonic slowness log.

Compressional and shear (V_P and V_S) velocities can also be used to estimate the elastic moduli of the formation. These moduli are used to infer mechanical properties of the formation at various depths that have applications not only in the petroleum industry, but also in civil and mining engineering and hydrogeology. The mechanical stiffness and strength of the formation are important parameters in the design of subsurface structures, nuclear waste disposal sites, and oil and gas pipelines. The dynamic Young's modulus Y and Poisson's

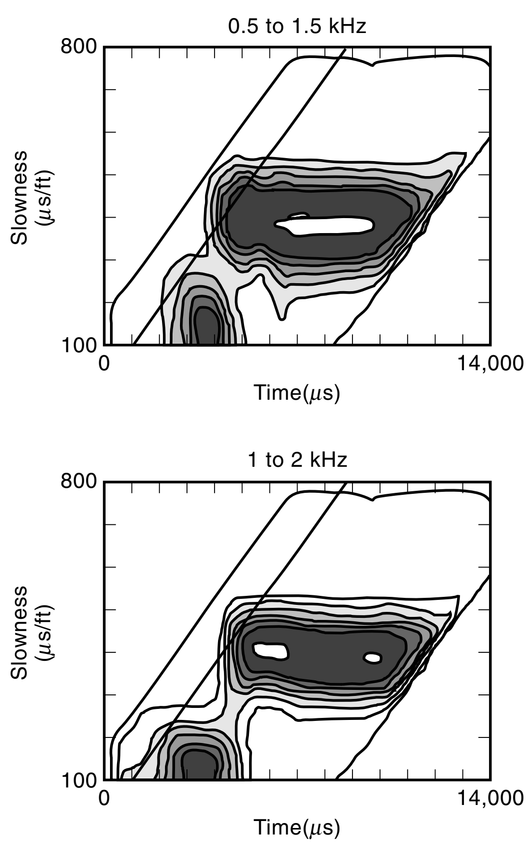

Figure 6. STC processing results for two processing windows at a given depth.

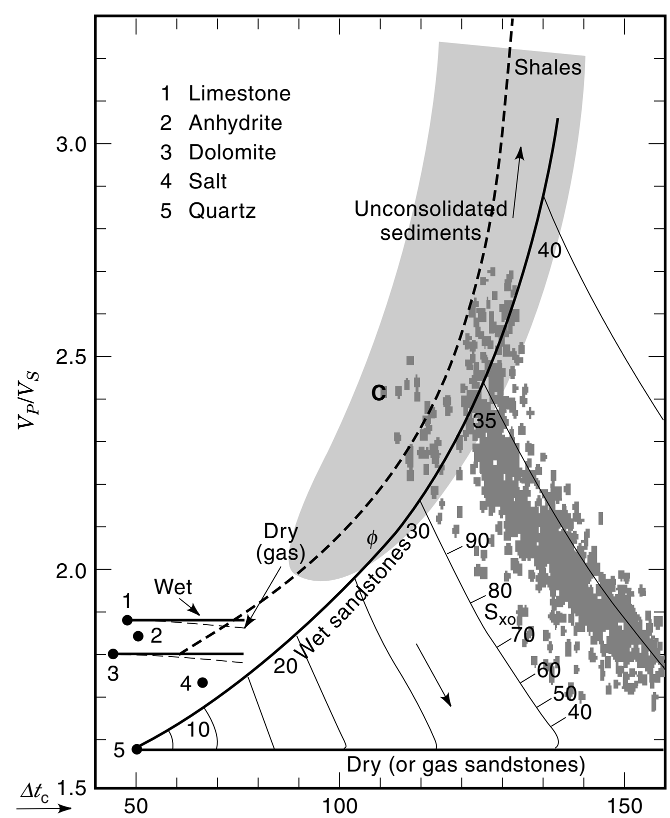

Figure 8. Correlations of V_P/V_S with Δt_c in μs/ft for different lithologies. Δt_c is proportional to the formation porosity.

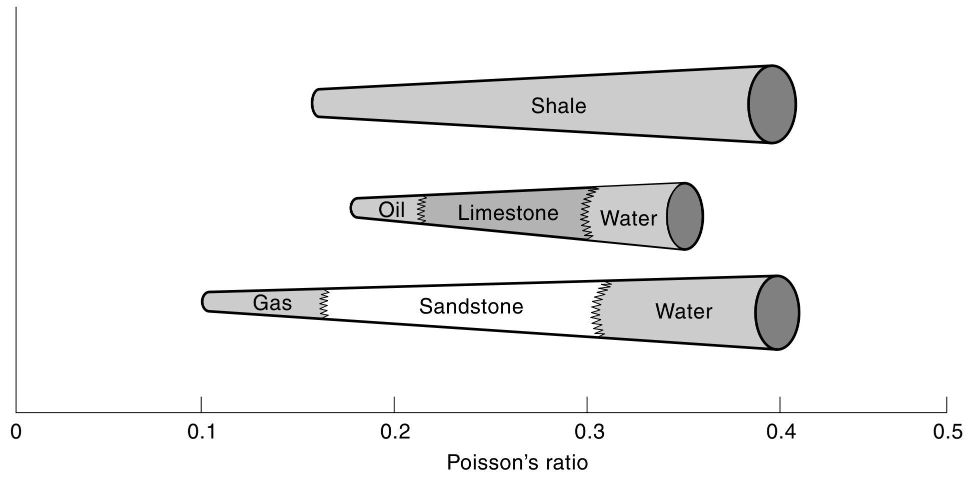

Figure 9. Range of Poisson's ratio for different lithologies.

ratio ν can be expressed in terms of the compressional and shear velocities by the following equations

$$Y = \rho V_S^2 \frac{[3(V_P/V_S)^2 - 4]}{[(V_P/V_S)^2 - 1]}$$

$$\nu = \frac{1}{2}\frac{[(V_P/V_S)^2 - 2]}{2[(V_P/V_S)^2 - 1]}$$

where ρ is the mass density of the formation at a given depth.

When the formation is not radialy homogeneous over the scale of measurement, it is of interest to estimate the effective radial depth of investigation in a conventional refracted head wave logging. This effective depth depends on the source-to-receiver spacings, the velocity contrast between the altered and undisturbed zones, and radial extent of the altered zone. The depth of investigation increases with source-to-receiver spacing and for increased velocity contrasts between the two zones (1).

Fracture Evaluation: Stoneley Reflections

A monopole Stoneley wave logging is also used to locate permeable fractures intersecting the borehole. The acoustic energy associated with the Stoneley wave is primarily located in the borehole fluid with gradual decay into the formation. The radial decay into the formation extends to about a wavelength. As a result, low-frequency Stoneley exhibits larger radial depth of investigation whereas high-frequency Stoneley is mostly confined to the borehole wall and propagates like an interfacial wave at the borehole fluid and formation boundary.

When a borehole Stoneley wave encounters an open fracture intersecting the borehole, some of its energy is reflected by the large acoustic impedance contrast created by the fracture. The ratio of the reflected to incident energy correlates with the openness of the fracture. This technique for the detection of permeable fractures works well in hard formations (9).

Permeability Indications: Stoneley Velocity and Energy Perturbations

Permeability is defined as the measure of how easily a fluid of certain viscosity flows through a rock under a pressure gradient. Permeability generally increases with porosity, grain size, and certain bedding patterns. In addition to fractures, Stoneley waves are also sensitive to formation permeability. The pressure pulse in the borehole fluid creates fluid movement into the surrounding formations with effective permeability. If the borehole wall is impermeable, the Stoneley wave travels without any attenuation caused by the radiation of acoustic energy into the formation. However, if the borehole crosses a permeable formation, the Stoneley wave attenuates by moving the fluid into the porous rock and its dispersive velocity decreases by varying amounts at different frequencies. Changes in the Stoneley dispersion over a reasonable bandwidth can be inverted for the formation permeability. This inversion is possible only if other parameters affecting the Stoneley dispersion are known from other measurements (10–12). In particular, Stoneley dispersion is also affected by borehole diameter and tool characteristics.

Formation Shear Logging

It is known that refracted shear head waves cannot be detected in slow formations (where the shear wave velocity is less than the borehole-fluid compressional velocity) with receivers placed in the borehole fluid.

Since formation shear wave velocity is of significant importance in determining formation lithology, recent effort has been directed toward logging borehole Stoneley and flexural modes for estimating formation shear wave velocity. Both of these borehole modes are the more energetic arrivals than the refracted headwaves. While a monopole source in a borehole primarily excites Stoneley mode, a dipole source is an efficient way of exciting borehole flexural waves. Stevens and Day (13) described a procedure for shear velocity logging in slow formations using the Stoneley dispersion. This procedure consists of inverting frequency-dependent Stoneley phase and group velocities together with attenuation for formation shear velocity. The inversion model is based on a sensitivity analysis described by Cheng et al. (14) for borehole Stoneley waves in terms of partial derivatives of Stoneley velocity with respect to model parameters. Stoneley velocity and attenuation are significantly affected by the permeability of poroelastic formations. Therefore, this procedure for determining shear velocity is applicable to essentially impermeable formations. On the other hand, borehole flexural waves are not as much affected by formation permeability and borehole fluid viscosity (12).

Even though flexural waves are easily excited in both the fast and slow formations over a bandwidth governed by its excitation function (15–18), it is a dispersive mode which is also influenced by four other model parameters (V_P, V_f, D, and ρ/ρ_f, where V_P is the formation compressional wave speed, V_f is the fluid compressional wave speed, D is the borehole diameter, and ρ/ρ_f is the ratio of the formation and fluid mass densities), besides the formation shear wave speed V_S. A sensitivity analysis of the flexural dispersion to small variations in the model parameters shows that the formation shear speed has by far the most dominant influence in a slow formation. In contrast, the flexural dispersion in a fast formation is significantly influenced by three of the five model parameters: the formation shear speed, the borehole fluid compressional speed, and the borehole diameter. The frequency dependence of these sensitivity functions indicates that the inversion of flexural dispersion for formation shear speed is optimal in the range 2 kHz to 4 kHz for a borehole of diameter 25.4 cm (19). The objective of flexural wave logging is to estimate the formation shear wave velocity from dipole waveforms recorded at an array of receivers. Kimball (20) has suggested one way of estimating the formation shear velocity from the processing of these waveforms. Processing of these waveforms by a variation of Prony's technique isolates both dispersive and nondispersive arrivals in the wavetrain (21). The Prony's spectral estimation technique consists of expressing the discrete frequency spectrum of an array of waveforms in terms of exponential functions for a given frequency. The exponential function contains the wavenumber of the associated mode at the selected frequency. The unknowns in the expansion consists of the amplitude and the exponential associated with each of the arrival. Consequently, even in the absence of any noise in the signal, the maximum number of arrivals that can be isolated is half the number of recorded waveforms. Several variations of the Prony's technique are available that can provide dispersions of various arrivals in the recorded waveforms. The low-frequency asymptote of flexural dispersion yields the formation shear velocity. It is also possible to invert a band-limited flexural dispersion for the formation shear velocity based on a sensitivity analysis as discussed by Sinha (19).

This inversion procedure attempts to estimate the formation shear velocity that would produce the measured dispersion over a given bandwidth. The procedure is based on obtaining a sensitivity matrix that relates fractional changes in phase velocity at various frequencies and model parameters from those at a reference state. The flexural dispersion in the reference state is known in terms of the assumed model parameters. The sensitivity matrix is calculated in terms of the known flexural wave solution in the reference state and a linearized perturbation model. Differences between the measured and reference flexural velocities at various frequencies can then be inverted for the estimated differences between the current and reference model parameters. Adding the difference in shear velocities (which is one of the model parameters) to the assumed value in the reference state yields the formation shear velocity that would produce the measured flexural dispersion. For simplicity, this discussion assumes that the remaining four model parameters in the current state are known from other sources and the formation shear velocity is the only unknown to be determined.

In addition to the five fundamental parameters, there are other environmental factors affecting acoustic waves propagating along a borehole. For instance, noncircular borehole geometry and altered zone surrounding the borehole with heterogeneities in material properties are two examples of environmental factors that may cause differences between the predicted modal dispersions obtained from the classical borehole model and those obtained from the processing of waveforms recorded in a borehole.

RECENT DEVELOPMENTS I: RADIAL ALTERATIONS

Radial alterations in formation properties (such as elastic wave velocities) may be caused by several sources, such as shale swelling, borehole overpressures, formation stresses, and mechanical damage (elastoplastic deformations) prior to brittle fractures. Under these circumstances, it is necessary to estimate the radial extent of such alterations as well as undisturbed formation velocities from sonic measurements made in a borehole.

When boreholes penetrate gas reservoirs with water-based mud, a fast mud-filtrate-invaded annulus is created near the borehole with slower gas reservoir existing beyond the annulus. In this situation, compressional headwaves propagating along the borehole typically probes only the mud filtrate. However, measurement of dispersive and leaky acoustic modes propagating in the annulus probe the undisturbed formation (gas reservoir) at low frequencies and annulus at high frequencies.

Recently, Burridge and Sinha (22) proposed a technique (based on Backus–Gilbert inversion) of inverting measured borehole flexural velocity dispersions for obtaining radial variation of formation shear velocity. This technique also provides information about the volume of investigation, amount of radial alteration, and undisturbed shear wave velocity in the far-field. The Backus–Gilbert (B–G) inversion technique yields an estimate of the radially varying formation shear velocity from a finite number of points on the flexural dispersion. It also indicates a trade-off relationship between the radial resolution and the error in the shear velocity estimate at different distances from the borehole. In the B–G technique a theoretical model predicts the corresponding changes in the dispersion relation caused by perturbations in the formation properties. This theoretical model is a perturbation scheme that relates changes in the borehole dispersions to changes in material parameters (19). This perturbation scheme is also used to carry out sensitivity analyses of borehole dispersions to various model parameters. Sensitivity analyses provide optimal bandwidths for inverting dispersion data for a particular material parameter. In slow formations, it has been shown that formation shear velocity is, by far, the most dominant parameter affecting the borehole flexural dispersion. Therefore, it is possible to invert measured flexural dispersions in slow formations for radial variation of shear velocity.

The B–G inversion technique consists of the following steps: Given flexural wave velocities at several discrete frequencies, a reasonable initial guess of the formation parameters is made. These initial parameters define the unperturbed (reference) state, which yields the "unperturbed" borehole flexural mode solution. The difference between the actual (or measured) and the unperturbed velocities at the axial wavenumbers corresponding to each of the data points constitute

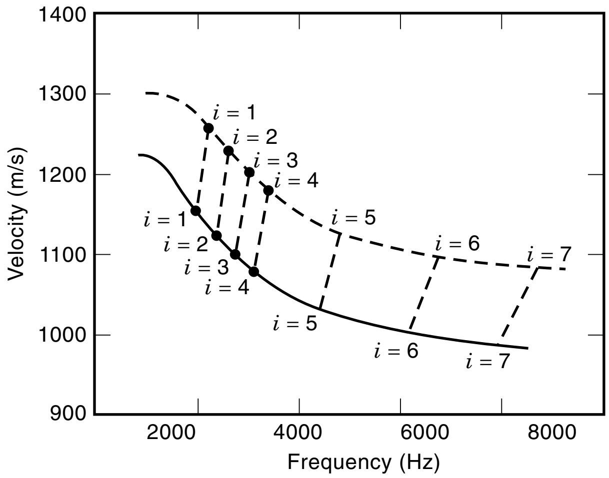

Figure 10. Flexural dispersions in the presence of a radial variation in shear velocity and that in the assumed homogeneous reference state.

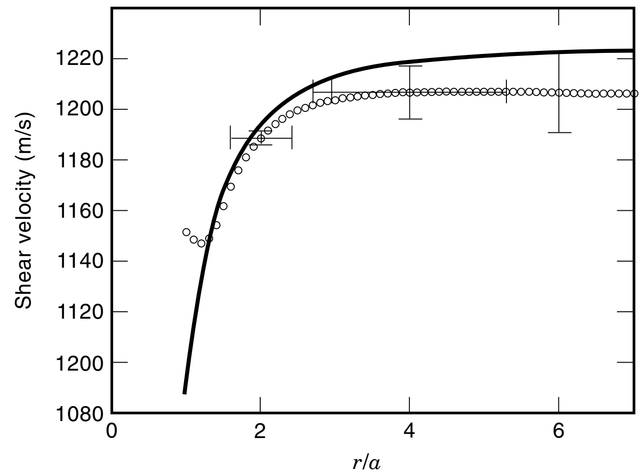

Figure 12. Inversion results for radial variation in formation shear velocity using velocity differences over a bandwidth of 2 kHz to 8 kHz and zero error in input velocities.

the input data to the B–G procedure. In addition, kernels are calculated from the "unperturbed" flexural model eigenfunctions for the reference medium. The sum of the inverted perturbation and the background profile yields the actual profile.

The solid and dashed lines in Fig. 10 denote borehole flexural dispersions in the presence of radial alteration in shear velocity and that in the selected homogeneous reference state, respectively. To invert flexural velocities at several discrete frequencies, we first calculate fractional changes in flexural velocities at corresponding wavenumbers that define the input to the B–G inversion model. The dashed line connecting the measured and reference dispersions are along constant wavenumbers. Note that it is necessary to select input data at frequency intervals of 500 Hz or more to ensure that they are uncorrelated. Figure 11 shows fractional changes in flexural velocities at seven frequencies ($i = 1, 7$) that serve as input to the B–G inversion model. Figure 12 displays the inversion results for radial variation in formation shear velocity using fractional changes in velocities shown in Fig. 12 over a bandwidth of 2 kHz to 8 kHz and zero error in input velocities. Figure 13 shows similar inversion results for the same input velocities but in the presence of a uniform error of 0.2% in input velocities.

Key features of this inversion model are that the accuracy and radial extent of inversion strongly depend on the bandwidth and accuracy of measured flexural dispersion. Since low- and high-frequency flexural waves have deep and shallow radial depths of investigation, respectively, it is preferable to have measured dispersion over as wide a bandwidth as possible.

RECENT DEVELOPMENTS II: FORMATION SHEAR ANISOTROPY

It is well recognized that sedimentary rocks are not, in general, elastically isotropic, but exhibit some degree of anisotropy. Anisotropy may arise intrinsic microstructural effects,

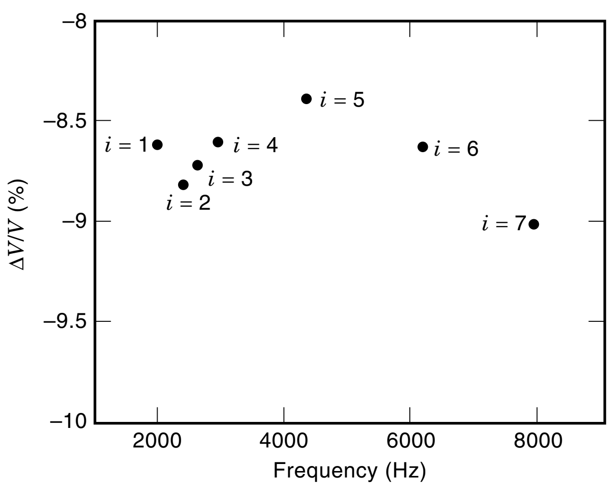

Figure 11. Velocity differences at fixed wavenumbers that are input to the Backus–Gilbert inversion.

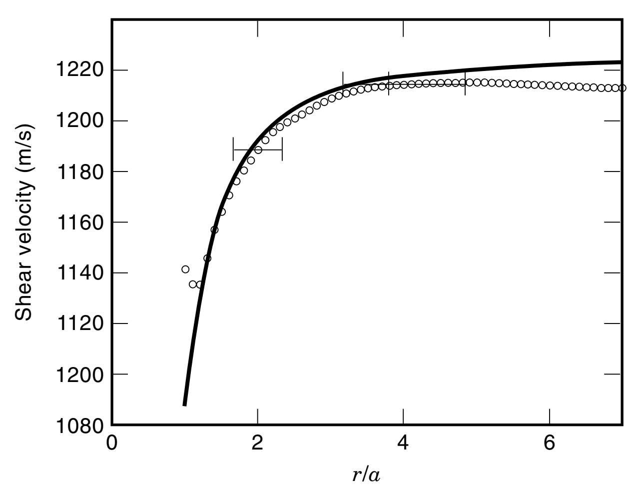

Figure 13. Inversion results for radial variation in formation shear velocity using velocity differences over a bandwidth of 2 kHz to 8 kHz and 2% error in input velocities.

such as layering of thin zones, or from local biaxial or triaxial tectonic stresses within the formation. Thomsen (23) provided a useful review of the measured anisotropy in many different rock types; based on the data, he concluded that most crustal rocks display weak anisotropy in many different rock types; based on the data, he concluded that most crustal rocks display weak anisotropy.

Bulk Wave Speeds in the Presence of Anisotropy

Consider an elastic solid of mass density ρ and arbitrary anisotropy; that is, it may have as many as 21 independent elasticity parameters. The equations of motion at circular frequency ω are (24)

$$\frac{\partial}{\partial x_j} C_{ijkl} e_{kl} + \rho\omega^2 u_i = 0 \tag{3}$$

Here u_i are the components of displacement, $i = 1, 2, 3$, and the summation convention on repeated subscripts is assumed. The strain components are $e_{ij} = (\partial u_i/\partial x_j + \partial u_j/\partial x_i)/2$, and the elastic moduli C_{ijkl} satisfy the general symmetries $C_{ijkl} = C_{jikl}$ and $C_{ijkl} = C_{klij}$, which are consequences of the symmetry of the stress tensor and the assumed existence of a strain energy function. The moduli can be succinctly represented by C_{IJ}, where the suffixes I and J run from 1 to 6, with $ij \leftrightarrow I$ according to 11, 22, 33, 23, 31, 12 $\leftrightarrow$ 1, 2, 3, 4, 5, 6.

Ignoring the borehole problem for the moment, we consider the propagation of plane waves in the formation, which for simplicity is assumed to be spatially uniform. Substituting the plane-wave solution $u_i = a_i \exp(i\omega n_j x_j/v)$ into Eq. (3), where $\boldsymbol{n}$ is the unit direction of propagation, and then multiplying by a_i, where $\boldsymbol{a}$ is the unit polarization vector, give an explicit expression for the phase speed v:

$$\rho v^2 = a_i a_k C_{ijkl} n_j n_l \tag{4}$$

The apparent simplicity of this expression is tempered by the difficulty of determining the polarization $\boldsymbol{a}$, which requires solving a 3×3 matrix eigenvalue problem, also known as the Kelvin–Christoffel equation (25). However, if the anisotropy is *weak,* then neither the eigenvalues nor the eigenvectors deviate much from their underlying isotropic counterparts. In particular, the polarization in Eq. (4) can be approximated by the equivalent isotropic polarization.

Consider a transversely isotropic (TI) material with axis of symmetry coincident with the x_3 direction. The five independent moduli are C_{11}, C_{33}, C_{13}, C_{44}, and C_{66}, such that

$$\boldsymbol{C} = \begin{bmatrix} C_{11} & C_{12} & C_{13} & 0 & 0 & 0 \\ C_{12} & C_{11} & C_{13} & 0 & 0 & 0 \\ C_{13} & C_{13} & C_{33} & 0 & 0 & 0 \\ 0 & 0 & 0 & C_{44} & 0 & 0 \\ 0 & 0 & 0 & 0 & C_{44} & 0 \\ 0 & 0 & 0 & 0 & 0 & C_{66} \end{bmatrix}$$

where $C_{66} = (C_{11} - C_{12})/2$. It is more convenient to work with the two moduli C_{33} and C_{44} and with three dimensionless anisotropy parameters, ϵ, η γ, each of which vanishes when the medium is isotropic:

$$\epsilon = \frac{C_{11} - C_{33}}{2C_{33}}, \quad \eta = \frac{C_{13} + 2C_{44} - C_{33}}{C_{33}}, \quad \gamma = \frac{C_{66} - C_{44}}{2C_{44}} \tag{5}$$

The parameters ϵ and γ were introduced by Thomsen (23); however, η is close to, but not exactly the same as, Thomsen's third anisotropy parameter, δ. The difference is discussed below.

The three wave speeds in a TI medium can be expressed in closed form (21). For instance, if $\boldsymbol{n} = (\sin\theta, 0, \cos\theta)$, then the exact expression for the SH phase speed is

$$\rho v_{\mathrm{SH}}^2 = C_{44}(1 + 2\gamma \sin^2\theta) \tag{6}$$

The identity in Eq. (6) follows directly from Eq. (4) and the fact that the SH polarization is $\boldsymbol{a} = (0, 1, 0)$. The formulae for the qSV and qP speeds are slightly more complicated, but well known (23). Since the qSV and qP polarizations must be in the $x_1 - x_3$ plane, both may be expressed in the form $(a_1, 0, a_3)$. Substituting into Eq. (4) yields

$$\begin{aligned} \rho v^2 = {} & C_{33}(a_1 \sin\theta + a_3 \cos\theta)^2 + C_{44}(a_1 \cos\theta - a_3 \sin\theta)^2 \\ & + 2C_{33} a_1 \sin\theta(\epsilon a_1 \sin\theta + \eta a_3 \cos\theta) \end{aligned} \tag{7}$$

If the anisotropy is *weak,* the qP polarization is almost $(\sin\theta, 0, \cos\theta)$, while the qSV is approximately $(\cos\gamma, 0, -\sin\theta)$. The discussion above implies that if these are used in Eq. (7), the result is a first-order approximation in ϵ and η to the phase speeds:

$$\rho v_{\mathrm{qP}}^2 = C_{33}[1 + 2\epsilon \sin^4\theta + 2\eta \sin^2\theta \cos^2\theta] \tag{8}$$

$$\rho v_{\mathrm{qSV}}^2 = C_{44}\left[1 + 2\frac{C_{33}}{C_{44}}(\epsilon - \eta)\sin^2\theta \cos^2\theta\right] \tag{9}$$

Because ϵ, η, and γ are small, one could use the approximation $(1 + x)^{1/2} \approx 1 + x/2$ for small x to get reasonable approximations to v_{SH}, v_{qP}, and v_{qSV} in weakly anisotropic TI media. The resulting expression for v_{SH} agrees with Eq. (16c) of Thomsen (23), but those for v_{qP} and v_{qSV} *do not* agree with the corresponding formulae in Thomsen (23), Eqs. (16a) and (16b). Perfect agreement is obtained if the substitution $\eta \to \delta$ is made, where

$$\delta = \frac{(C_{13} + C_{44})^2 - (C_{33} - C_{44})^2}{2C_{33}(C_{33} - C_{44})} \tag{10}$$

Thomsen (23) derived the approximate wavespeeds for the TI medium by explicit expansion of the known expressions for the speeds, and he was led by this route to the nondimensional parameter δ. It is clear from the algebraic identity

$$\delta = \eta + \frac{\eta^2}{2\left(\dfrac{C_{33}}{C_{44}} - 1\right)}$$

that η is slightly smaller than δ but the two parameters are interchangeable in the limit of weak anisotropy; their difference is of second order. Hence, the differences between these results and Thomsen's are of second order in the anisotropy.

In his paper, Thomsen (23) demonstrated that δ (and hence η) is of critical significance to exploration geophysics, but that it is "an awkward combination of elastic parameters." Because of its simpler form [compare Eqs. (5) and (10)], Norris and Sinha (24) suggest that η rather than δ be used as a measure of anisotropy.

Borehole Modes

Acoustic anisotropy in rocks can be divided into two broad categories: intrinsic and stress-induced. The motivation for this classification stems from differences in the response of elastic waves propagating along a borehole in a formation with intrinsic or stress-induced anisotropy. The response of acoustic waves in anisotropic materials can be described in terms of effective elastic constants in the equations of motion. These constants are derived from a microscopic description of the material that can have certain crack distributions or thin layers of different elastic properties. When the elastic properties are appropriately averaged over a finite volume of the rock with cracks or layerings, the effective elastic constants exhibit orthohombic or TI symmetry. Two commonly encountered situations involve a fluid-filled borehole traversing a formation with the TI symmetry axis perpendicular (TIH) and parallel (TIV) to the borehole axis. Vertically aligned fractures and inclusions, as well as biaxial horizontal stresses surrounding a vertical borehole, give rise to an effective formation with the TIH (TI anisotropy with a horizontal axis of symmetry) anisotropy. On the other hand, intrinsic anisotropy of horizontal shale layerings and anisotropy caused by horizontal find beddings represent an effective formation with the TIV (TI anisotropy with a vertical axis of symmetry) anisotropy. In a TIV formation, there is only one shear velocity for waves propagating up the borehole. In contrast, there are two shear waves with different velocities that can propagate along the borehole in a TIH formation. The difference in the two shear velocities is typically measured with orthogonal dipole sources and receiver pairs placed on the borehole axis.

The Tube Wave Speed in Anisotropic Formations

A monopole source placed on the borehole axis produces the lowest-order axisymmetric (Stoneley) wave propagating along the borehole. This is a dispersive wave whose low-frequency asymptote coincides with the tube wave speed. Closed-form expression for the tube wave speed in anisotropic formations is of value in inverting for a certain combination of formation anisotropic constants.

Consider a circular borehole, $r < a$ in cylindrical coordinates (r, ϕ, x_3), which is occupied by an inviscid fluid of density ρ_f and bulk modulus $K_f = \rho_f v_f^2$, where v_f is the fluid wave speed. The formation, $r > a$, is an arbitrary anisotropic solid, and for simplicity it is assumed to be spatially uniform. The tube wave is the quasi-static or limiting low-frequency form of the azimuthally symmetric Stoneley wave mode in an isotropic formation with speed given by (15)

$$v_T = v_f \left(1 + \frac{K_f}{\mu}\right)^{-1/2} \tag{11}$$

where μ is the formation shear modulus. The displacement field in the formation is proportional to the plane strain displacement that results from an applied uniform pressure, say p, on $r = a$. The static displacement for $r > a$ is (15)

$$u_\alpha = \frac{pa^2}{2\mu}\frac{x_\alpha}{r^2}, \quad \alpha = 1, 2; \qquad u_3 = 0 \tag{12}$$

Norris and Sinha (24) have shown that the tube wave speed in a weakly anisotropic formation is v_T given by Eq. (11), where the *effective* shear modulus for the formation is μ^*, which is given by

$$\mu^* = \tfrac{1}{8}(C_{11} + C_{22} - 2C_{12} + 4C_{66}) \tag{13}$$

This expression for the effective shear modulus is not restricted to any particular material symmetry and is equally valid for a triclinic or a TI formation.

Norris and Sinha (24) have discussed inversion of a subset of formation anisotropic constants from borehole measurements under the assumption that the orientation of the borehole axis with respect to the TI symmetry axis is known.

Dipole Shear Anisotropy Logging

Generally, the goal of dipole shear anisotropy logging is to identify and characterize (a) aligned fractures in hard (fast) formations, (b) intrinsic anisotropy in shales because of microlayerings, and (c) stress-induced anisotropy in tectonically active formations (26–28). Esmersoy et al. (29) have described the details of dipole shear anisotropy logging. Processing of recorded waveforms at the two pairs of orthogonal receivers produced by two orthogonal dipole sources yields the azimuthal orientation of (a) the fast shear direction and (b) the fast and slow shear wave slownesses (or velocities). When the borehole axis is perpendicular to the TI symmetry axis, the fast shear direction coincides with the fracture strike in the presence of fracture-induced shear anisotropy. The difference between the fast and slow shear wave velocities (also referred to as the magnitude of shear anisotropy) is related to the transverse fracture compliance as described by Schoenberg and Sayers (30):

$$\rho_b(V_{12}^2 - V_{13}^2) = \mu_b \delta_T \tag{14}$$

where ρ_b and μ_b are the mass density and shear modulus of the background medium; V_{12} and V_{13} are the fast and slow shear wave velocities with X_1 as the propagation direction; and X_2 and X_3 as the shear polarization directions, respectively. δ_T is the transverse fracture compliance, and fractures are in the X_1–X_2 plane. $Z_T = 4S_{44}$ is the tangential compliance of the fractured medium.

When the borehole axis makes an arbitrary angle with respect to the TI symmetry axis of the formation, the effective anisotropy exhibits monoclinic symmetry with respect to the borehole measurement axis. Under these circumstances, borehole flexural dispersions for the fast and slow dipole orientations exhibit characteristic differences in fast (Bakken shale) and slow (Austin chalk) formations as discussed by Sinha et al. (27) and by Leslie and Randall (31). The differences in

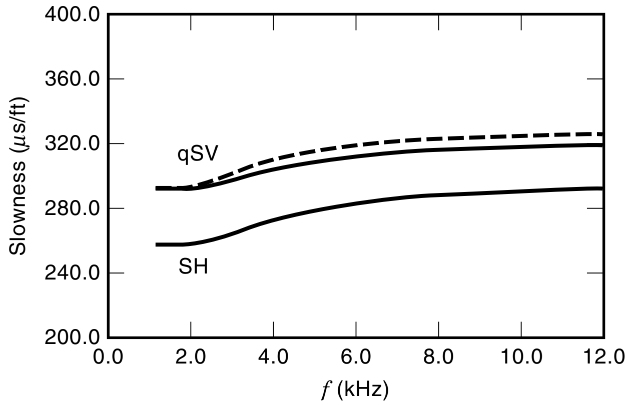

Figure 14. Borehole flexural dispersions for the fast and slow radial polarization directions in a TIH formation (Austin chalk). The water-filled borehole diameter is 8 in. (20.32 cm). The dashed and solid lines denote results from an equivalent isotropic and anisotropic models, respectively.

flexural dispersions are shown in Figs. 14 and 15 for Bakken shale and Austin chalk for the case of borehole axis perpendicular to the TI symmetry axis TIII anisotropy).

Note that the fast and slow flexural dispersions have a tendency to merge together at higher frequencies in the case of fast formations. In contrast, the two dispersions are approximately parallel to each other in the case of slow formations.

Sinha et al. (27) have shown that for weakly anisotropic formations, it is possible to define two equivalent isotropic formations with approximately the same flexural dispersions as that of the fully anisotropic formations. The two equivalent isotropic formations are defined by the actual compressional (qP) and the fast (SH) or slow (qSV) shear wave velocities along the borehole axis. The dashed curves in Figs. 14 and 15 denote borehole flexural dispersions obtained from the equivalent isotropic formations. Agreement is well within 1% to 2% between the equivalent isotropic and fully anisotropic formation results. This is an important result because it forms the basis for the processing of dipole dispersions in anisotropic formations. This processing consists of Alford rotation of the cross-dipole waveforms at a given depth for identifying the fast and slow shear directions (32). The inline waveforms corresponding to the fast and slow dipole orientations are then subjected to semblance processing for obtaining the fast and slow shear slownesses as described by Kimball and Marzetta (8) and Esmersoy et al. (29).

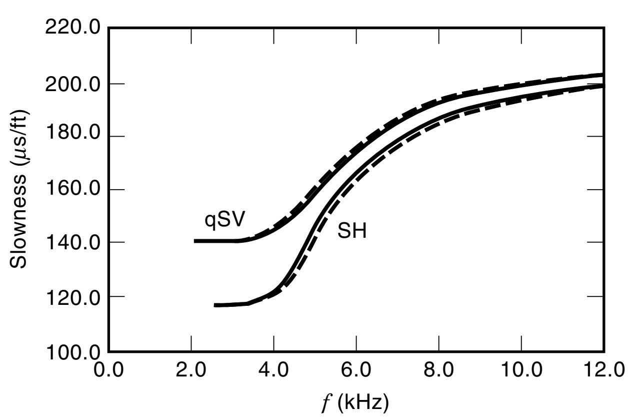

Figure 15. Borehole flexural dispersions for the fast and slow radial polarization directions in a TIH formation (Bakken shale). The water-filled borehole diameter is 8 in. (20.32 cm). The dashed and solid lines denote results from an isotropic and anisotropic models, respectively.

RECENT DEVELOPMENTS III: SONIC MEASUREMENTS IN THE PRESENCE OF FORMATION STRESSES

Formation stresses play an important role in geophysical prospecting and development of oil and gas reservoirs. Both the direction and magnitude of these stresses are required in (a) planning for borehole stability during directional drilling, (b) hydraulic fracturing for enhanced production, and (c) selective perforation for prevention of sanding during production.

Figure 16 shows a geologic cross section of Cusiana fields in Colombia. Hydraulic thrust from the Pacific Ocean onto a tectonic plate produces horizontal stresses in formations. Such horizontal stresses, together with the vertical overburden stress, constitute the formation stresses. The formation stress state is characterized by the magnitude and direction of the three principal stresses. Generally, the overburden pressure yields the principal stress in the vertical direction. The magnitude of vertical stress is known by integrating the mass density of formation from the surface to the depth of interest. Consequently, identifying the other two principal stresses is the remaining task necessary to fully characterize the formation stress state.

When drilling horizontal wells, it is critical to know the subsurface stress. A well drilled in the wrong direction may suffer from premature collapse. Stress information is used in the drilling and completion of horizontal wells, especially in the areas of fractured reservoirs. Figure 17 illustrates various choices in planning horizontal well orientations with respect to the principal stress directions. A stable horizontal well direction is the one that causes minimal stress differential between the maximum and minimum stresses in the azimuthal plane perpendicular to the drilling direction.

Stress affects the velocity of elastic, small-amplitude waves by varying amounts depending on the material nonlinearity. The dependence of the acoustic wave velocity on biasing stresses in the propagating medium is known as acoustoelasticity. Figure 18 shows a schematic diagram of a liquid-filled borehole of radius a in a formation subject to a uniaxial stress S. The measurement system consists of a piezoelectric source and an array of hydrophone receivers.

The propagation of small amplitude waves in homogeneous and anisotropic solids is governed by the linear equations of motion. However, when the solid is prestressed, the propaga-

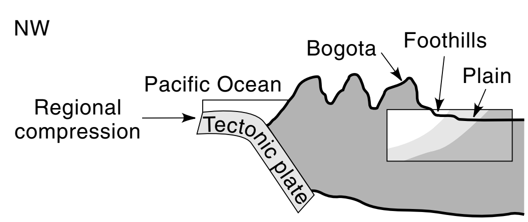

Figure 16. A geologic cross section of the Cusiana fields in Colombia.

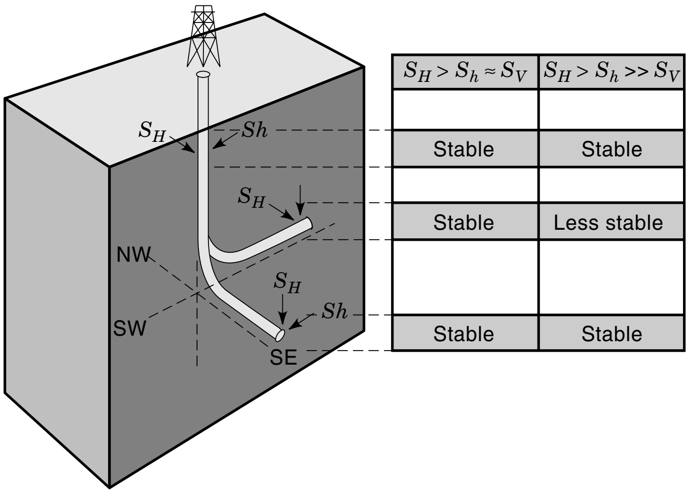

Figure 17. Examples of horizontal wells and formation stresses.

tion of such waves are properly described by equations of motion for small dynamic fields superposed on a static bias (28). A static bias represents any statically deformed state of the medium due to an externally applied load or residual stresses.

Dipole sonic logging tools can measure azimuthal anisotropy in the surrounding formation (29,33). However, measurements are typically done at low frequencies (in the range of 1 kHz to 5 kHz) with the goal of estimating azimuthal shear anisotropy. At these low frequencies, flexural waves have larger radial depth of investigation and are not significantly affected by the stress-induced altered zone extending to about one borehole diameter. There is no difference in the azimuthal shear anisotropy caused by either intrinsic sources or stress-induced sources that are obtained from the low-frequency asymptotes of flexural wave speeds. However, at higher frequencies (in the range of 5 kHz to 10 kHz in moderately fast formations and in the range of 2 kHz to 5 kHz in slow formations in a typical borehole diameter of 20.32 cm), flexural waves become largely sensitive to the stress-induced altered zone close to the borehole. This stress-induced altered zone exhibits acoustic velocity heterogeneities in the two principal stress directions. Other types of formation anisotropy that are typically described by a TI medium do not exhibit

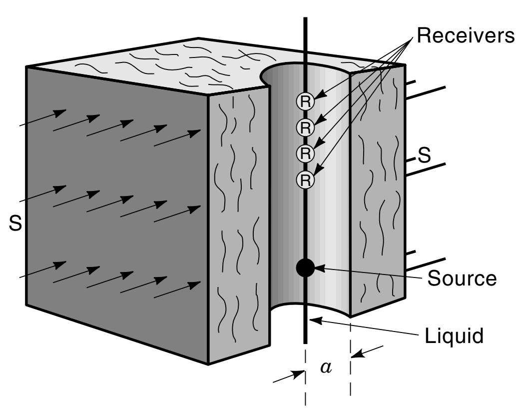

Figure 18. A fluid-filled borehole in a uniaxially stressed formation.

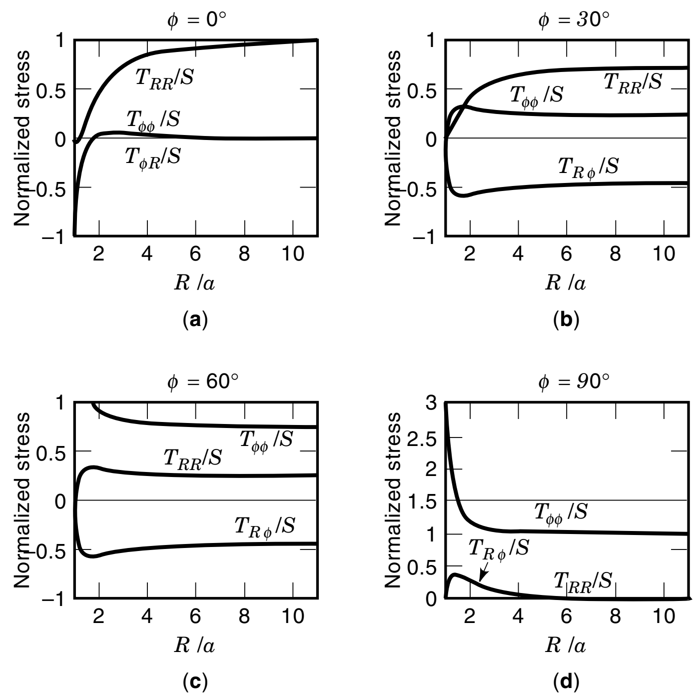

Figure 19. Stress distributions in the vicinity of a borehole.

any such acoustic velocity heterogeneity in the radial direction (27).

Figure 19 displays the radial (T_{RR}), tangential or hoop ($T_{\phi\phi}$), and radial–azimuthal shear ($T_{R\phi}$) stress distributions. These stresses exhibit significant variations in an annulus extending up to approximately three times the borehole diameter. The radial heterogeneity in acoustic wave velocity in this annulus is a result of borehole stress concentration and is not found in intrinsically anisotropic formation. Beyond this annulus, the stress is essentially the tectonic uniaxial stress. Note that T_{RR} vanishes at the borehole surface because we assume that there is no static pressure in the borehole fluid.

The stress distributions shown in Fig. 19 can be transformed into a corresponding plane wave velocity distribution for any point (R and ϕ) in the azimuthal plane as described by Sinha and Kostek (28). Appendix B of Ref. 28 provides expressions for the plane wave velocities in terms of principal stresses and strains in any material together with its linear (second-order) and nonlinear (third-order) elastic constants. However, the near borehole stresses are, generally, expressed in terms of polar coordinates (R and ϕ) that are not coincident with the principal stress axes in the far-field for all values of ϕ. Therefore, it is necessary to rotate the stresses at an arbitrary point (R, ϕ) by $-\phi$, so that all the stresses are referred to the principal axes defined by the far-field stresses.

Under the above-mentioned plane strain assumption, the resulting expressions for the compressional and shear wave velocities for waves propagating along the X_1 direction in an isotropic medium subject to homogeneous normal stress S along the X_2 direction in the far-field are given by

$$\rho_0 V_{11}^2(R,\phi) = \lambda + 2\mu + \left[\nu + \frac{(1-2\nu)c_{112}}{2\mu}\right](T_{RR} + T_{\phi\phi}) \quad (15)$$

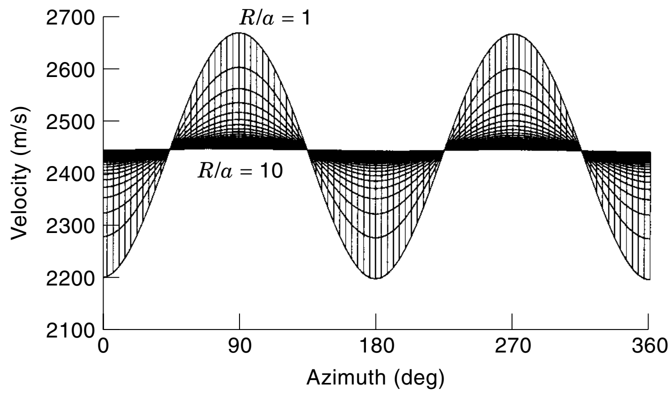

Figure 20. Compressional wave velocity distribution in the vicinity of a borehole.

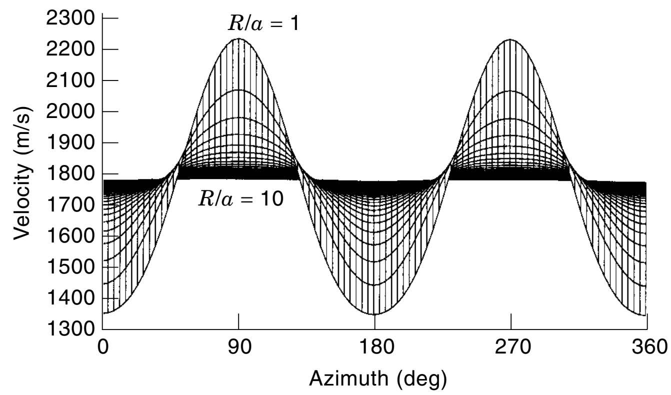

Figure 21. Fast shear wave velocity distribution in the vicinity of a borehole.

$$\rho_0 V_{12}^2(R,\phi) = \mu - \frac{\nu}{2\mu}(c_{144}+c_{155})(T_{RR}+T_{\phi\phi}) + \left(1+\frac{c_{155}}{2\mu}\right) T'_{RR} + \frac{c_{144}}{2\mu}T'_{\phi\phi} \tag{16}$$

$$\rho_0 V_{13}^2(R,\phi) = \mu - \frac{\nu}{2\mu}(c_{144}+c_{155})(T_{RR}+T_{\phi\phi}) + \left(1+\frac{c_{155}}{2\mu}\right) T'_{\phi\phi} + \frac{c_{144}}{2\mu}T'_{RR} \tag{17}$$

where

$$T'_{RR} = T_{RR}\cos^2\phi + T_{\phi\phi}\sin^2\theta - T_{R\phi}\sin 2\phi \tag{18}$$

$$T'_{\phi\phi} = T_{RR}\sin^2\phi + T_{\phi\phi}\cos^2\phi + T_{R\phi}\sin 2\phi \tag{19}$$

In Eqs. (15) to (17), ρ_0 is the mass density in the reference state; T_{RR}, $T_{\phi\phi}$, and $T_{R\phi}$ are the stresses in polar coordinates; and $c_{144} = \frac{1}{2}(c_{112} - c_{123})$ and $c_{155} = \frac{1}{4}(c_{111} - c_{112})$ are the nonlinear constants. We follow the convention that V_{IJ} denotes the plane wave velocity for propagation along the X_I direction and polarization along the X_J direction.

Figure 20 shows azimuthal variation of compressional wave velocity V_{11} at several radial distances from the borehole surface (R/a = 1, 1.2, 1.4, . . ., 10) for propagation parallel to the borehole (X_1) axis. The uniaxial stress is applied parallel to the X_2 axis and its magnitude $S = -5$ MPa. The formation material constants used in these calculations are listed in Table 1. Figure 21 shows a similar plot (as in Fig. 20) for the fast shear wave velocity V_{12} for propagation in the X_1 direction and polarization in the X_2 direction which is parallel to the applied uniaxial stress. The far-field shear wave velocity V_{12} is approximately 1790 m/s^2 for R/a = 10.

Shown in Fig. 22 is a similar plot (as in Fig. 20) for the slow shear wave velocity V_{13} for propagation in the X_1 direction and polarization in the X_3 direction which is perpendicular to the applied uniaxial stress. The far-field shear wave velocity V_{13} is approximately 1640 m/s^2 for R/a = 10.

Table 1. Material Properties for a Dry Berea Rock

ρ_0 (kg/m^3)	V_S (m/s)	V_P/V_S	c_{111} (GPa)	c_{112} (GPa)	c_{123} (GPa)
2062	1500	1.55	−21,217	−3044	2361

Crossover in Flexural Dispersions

When the biasing state of the propagating medium is known and the flexural wave solution, in the absence of any uniaxial stress, is calculated in the reference state, the changes in the flexural wave dispersion due to any given biasing stress distributions can be calculated from a perturbation equation as described by Sinha and Kostek (28).

We have computed tectonic stress-induced changes in flexural wave dispersions for a borehole of diameter 0.2 m (8 in.) surrounded by a formation. The formation material properties are listed in Table 1. The material constants were estimated from acoustic velocity measurements made on a uniaxially stressed sample at 5 MPa. We have chosen c_{111}, c_{112}, and c_{123} in the compressed Voigt notation to be the three independent third-order elastic constants of an isotropic formation in the absence of any nonhydrostatic stress in the reference state. The nonlinearity parameter is defined as $\beta = (3c_{11} + c_{111})/2c_{11}$, where $c_{11} = \rho v_p^2$, is -954 for this formation. This nonlinearity parameter for rocks varies by several orders of magnitude depending on the rock type, porosity, degree of compaction, and so on. Generally, slower formations exhibit higher degree of nonlinearity than faster ones.

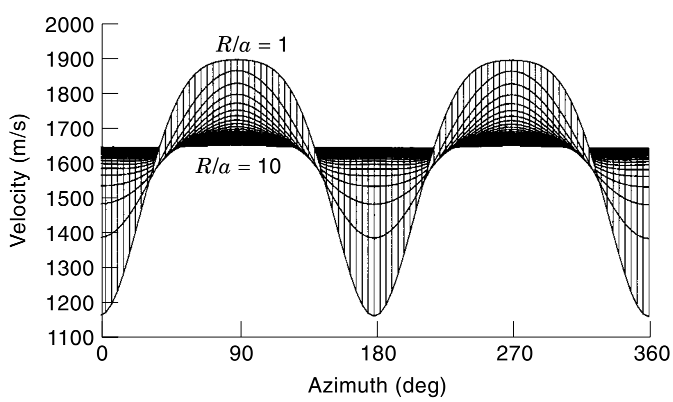

Figure 22. Slow shear wave velocity distribution in the vicinity of a borehole.

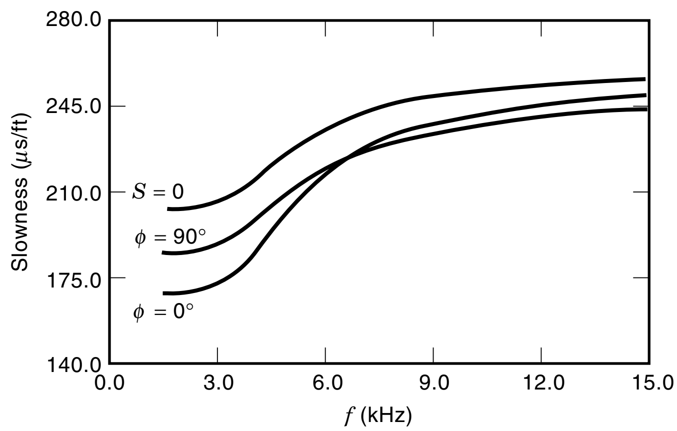

Figure 23. Borehole flexural dispersions for the fast ($\phi = 0°$) and slow ($\phi = 90°$) radial polarization directions in a uniaxially stressed formation. The flexural dispersion crossover is an indicator of stress-induced azimuthal anisotropy.

In addition, we assume a borehole fluid with a compressional wave velocity $V_f = 1500$ m/s and mass density $\rho_f = 1000$ kg/m^3.

In Fig. 23 we show the flexural wave velocity dispersion with and without a uniaxial compressive stress of 5 MPa (725 psi). The angle ϕ denotes the orientation of the radial component of the flexural wave relative to the uniaxial stress direction. Note that when the radial component is parallel to the uniaxial compressive stress direction ($\phi = 0°$), the flexural wave velocity significantly increases from the unstressed case at low frequencies. On the other hand, when the radial component is normal to the stress direction ($\phi = 90°$), the velocity again increases, but by a lesser amount at low frequencies. It is clear from Figs. 21 and 22 that V_{12} is larger than V_{13} for $R/a = 10$ that corresponds to the far-field. However, V_{13} is larger than the unstressed shear wave speed of 1500 m/s, because of the formation nonlinear constants used and the far-field compressive stress which is now perpendicular to the shear polarization direction. In some other materials with different magnitudes of third-order elastic constants, it is possible to have V_{13} lower than the unstressed shear wave speed. At low frequencies, the radial polarization of flexural waves with higher velocity coincides with the far-field stress direction S. However, as the frequency increases, flexural wave velocity dispersions for the two cases $\phi = 0°$ and $\phi = 90°$ cross each other; and beyond the crossover frequency, the flexural wave velocity corresponding to $\phi = 90°$ becomes higher than that for $\phi = 0°$. This reversal in the relative values of the velocities for the two polarization directions is characteristic of uniaxial stress-induced azimuthal anisotropy, a result of the drilling of the borehole. This near-borehole effect is observable only at relatively high frequencies (typically between 5 kHz and 10 kHz for a borehole of diameter 0.2 m). At these frequencies, the wavelength is smaller than the borehole diameter. The fractional change in flexural wave velocities is quite large (approximately 10°) at low frequencies, whereas the difference reduces to about 2% at high frequencies. Dipole sonic tools can measure flexural wave speeds with a resolution of 1% to 2%. It should also be carefully noted that these differences are for the assumed values of the formation parameters and a somewhat low magnitude of uniaxial stress (5 MPa). Recent measurements on a laboratory sample of slower and softer rock indicate that these differences at both low and high frequencies can be on the order of 6% to 8% for a uniaxial compressive stress of 5 MPa (34,35).

It is clear from Fig. 23 that the relative magnitude of the flexural wave velocities for the fast and slow dipole source directions reverse at very high frequencies from those at low frequencies, which results in a flexural dispersion crossover. This crossover phenomenon is, evidently, caused by the borehole stress concentration. An effective stress–concentration annulus width is approximately equal to the borehole diameter. Radial distributions of seismic shear wave velocities for polarizations parallel and normal to the far-field stress direction also show a crossover at the edge of this annulus. The crossover frequency in the fast and slow flexural dispersions occurs when the wavelength approximately equals the borehole diameter. To a lesser degree, the crossover frequency is also affected by the formation material nonlinearity and stress magnitude.

Shear Stress Parameter

Under the assumption that the observed azimuthal shear velocity anisotropy is due solely to the uniaxial tectonic stress, one can estimate the largest formation shear stress parameter from the expression (28)

$$\rho_0(V_{12}^2 - V_{13}^2) = \left(1 + \frac{c_{456}}{c_{66}}\right) 2T_{23}^{\max} \tag{20}$$

where ρ_0 is the formation mass density; $c_{456} = (c_{111} - 3c_{112} + 2c_{123})/8$, a third-order elastic constant of the formation in the reference state; V_{12} and V_{13} are the low-frequency velocities for flexural waves propagating along X_1 direction, with radial polarizations along the X_2 and X_3 directions, respectively. Note that at these low frequencies, the flexural wave velocities asymptotically approach shear wave velocities with polarizations parallel to the radial component of the borehole flexural wave. The quantities on the left-hand side of Eq. (20) can be obtained from the formation mass density in the reference state and the shear wave anisotropy estimated either from the low-frequency asymptotes of borehole flexural wave velocities or from shear wave velocities for the two principal polarization directions from borehole seismic measurements. The quantity on the right-hand side is the formation shear stress parameter in the azimuthal plane normal to the borehole axis. If the formation nonlinear constant c_{456} is known, the maximum shear stress magnitude or, equivalently, the difference between the maximum and minimum tectonic stresses in the azimuthal plane can be obtained from Eq. (20). We note that for rocks with large acoustoelastic coefficients, $|c_{456}/c_{66}| \gg 1$. As a result, these rocks exhibit large stress-induced azimuthal anisotropy in shear wave velocities for the two principal polarization directions for a given difference in the stress magnitudes ($T_{22} - T_{33}$) in the azimuthal plane.

The principal stress directions in the azimuthal plane are aligned along the shear polarization directions that correspond to the highest and lowest flexural wave velocities at low frequencies. The direction of the largest formation shear stress is oriented 45° from one of the principal axes in the azimuthal plane.

In summary, the presence of a borehole significantly alters the existing stress state in the near-field. These borehole stresses introduce characteristic frequency dependencies of flexural wave velocities as a function of the polarization direction. At low frequencies, the flexural wave velocities asymptotically approach the shear wave velocities in the formation with the same polarization. The fast flexural wave polarization direction coincides with the far-field stress direction. On the other hand, at high frequencies the first flexural wave polarization direction is perpendicular to the far-field stress direction. This behavior is due to the stress concentration around the borehole and is unique to stress-induced azimuthal anisotropy. This flexural dispersion crossover in the wave velocities for the two orthogonally polarized flexural waves is not observed in intrinsically anisotropic formations. Consequently, this flexural wave characteristic provides a technique to distinguish stress-induced anisotropy from other sources of formation anisotropy. The possibility of this technique for identifying stress-induced anisotropy in formations was first predicted by a theoretical analysis of stress-induced effects on borehole flexural waves (28). Experimental verification of the flexural dispersion crossover in uniaxially stressed laboratory samples has been reported by Sinha et al. (34) and Winkler et al. (35). While the nonlinearity parameters of rocks may vary by several orders or magnitude with substantially different acoustoelastic effects, we note that stress-induced effects on borehole flexural waves are, generally, larger in slower and softer rocks. Once the flexural anisotropy is attributed to the stress in the formation, the fast shear polarization direction can be interpreted to be the far-field uniaxial stress direction. Moreover, the asymptotic behavior of flexural waves at low frequencies can be utilized to estimate the largest shear stress parameter that is potentially useful in the estimation of the mechanical properties of the formation around the borehole.

RECENT DEVELOPMENTS IV: FORMATION NONLINEAR CONSTANTS

Nonlinearities in rocks cause stress dependence of acoustic wave velocities. The nonlinear constitutive relations of such isotropic materials are described in terms of two linear and three nonlinear elastic constants. Acoustic time waveforms recorded at two different borehole pressures can be used to estimate two of the three formation nonlinear constants. Processing of these time waveforms produced by a monopole or dipole source yields the Stoneley or flexural dispersions, respectively. The differences in the Stoneley and flexural dispersions caused by a known change in the borehole pressure are then utilized in a multifrequency inversion model that yields two of the three independent nonlinear constants of the formation. These two nonlinear constants, c_{144} and c_{155}, are sufficient to calculate the difference between the maximum and minimum stresses in the azimuthal plane from the dipole anisotropy in the fast and slow shear wave velocities. In addition, they are also sufficient to compute the stress derivatives of shear wave velocities in a uniaxially stressed sample of the same material as that of the in situ formation. Generally, a positive derivative indicates that the rock sample would stiffen, and a negative derivative indicates that it would soften with increasing uniaxial stress.

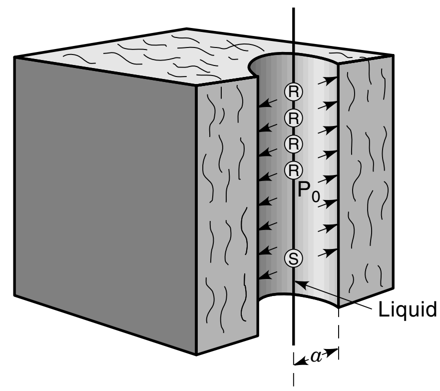

Figure 24. A pressurized borehole with an acoustic source and an array of receivers.

Stoneley and Flexural Dispersions

Figure 24 shows a diagram of a borehole of radius a, taken here as 10.16 cm (4 in.). When the borehole pressure is increased by P_0 above the ambient pressure, static deformations of the borehole fluid and formation are described by the static equations of equilibrium and continuity of radial component of particle displacement and radial stress at the borehole wall. Figure 25 shows the radial and hoop stress distributions away from the borehole. The influence of these static stresses on the propagation of borehole modes is studied in some detail by Sinha et al. (36). Table 1 contains a summary of the material constants in the ambient state that were used in the calculations for the Stoneley and flexural dispersions before and after an increase in the borehole pressure by P_0. Here ρ_0 is the formation mass density; c_{111}, c_{112}, and c_{123} are the three third-order elastic constants for a dry Berea rock written in Voigt compressed notation; $c_{144} = (c_{112} - c_{123})/2$; and $c_{155} = (c_{111} - c_{112})/4$. At the ambient pressure, the borehole fluid is assumed to have a compressional wave velocity $V_f = 1500$ m/s; mass density $\rho_f = 1000$ kg/m^3; and its nonlinearity parameter $B/A = 5$ (37).

An increase in the borehole pressure causes changes in the material properties of the borehole fluid and formation that

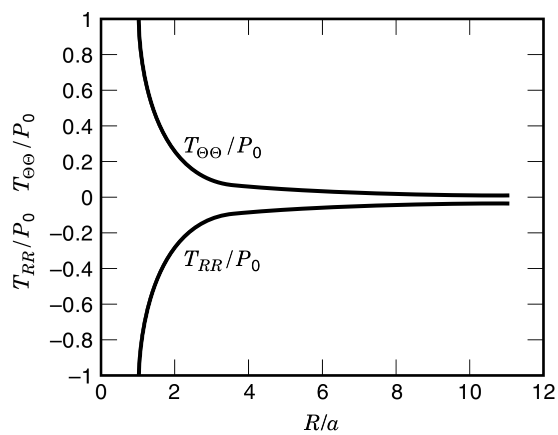

Figure 25. Incremental stress distributions in the borehole vicinity caused by an increase in borehole pressure P_0. T_{RR} and $T_{\theta\theta}$ are the radial and hoop stresses, respectively.

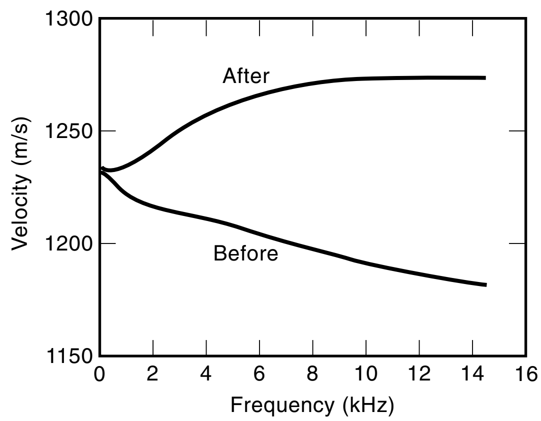

Figure 26. Borehole Stoneley dispersions before and after an increase in borehole pressure $P_0 = 5$ MPa.

are calculated in terms of the fluid and formation nonlinear constants. So both the fluid and formation nonlinearities contribute to the pressure-induced changes in the Stoneley and flexural dispersions. Figure 26 displays the Stoneley dispersions in the ambient state and after an increase in the borehole pressure by $P_0 = 3.447$ MPa (500 psi).

Figure 27 shows the flexural dispersions before and after pressurization. Both the Stoneley and flexural dispersions in the ambient state are obtained from the solution of a standard boundary-value problem. After an increase in the borehole pressure, the corresponding dispersions are obtained from a previously reported perturbation model (36). Since the formation nonlinearities for a dry Berea sandstone are significantly larger than that of borehole fluid, the contribution of fluid nonlinearity to the pressure-induced changes in the Stoneley and flexural dispersions is minimal.

Sensitivity of the Stoneley Dispersion to the Nonlinear Constants

The sensitivity of the two formation nonlinear constants (normalized by its shear modulus c_{66}), $N_1 = -c_{144}/c_{66}$, and $N_2 = -c_{155}/c_{66}$ to the Stoneley dispersion caused by an increase in the borehole pressure can be studied from a previously reported perturbation analysis (36). This perturbation analysis relates a fractional change in the Stoneley wave velocity at various frequencies to a corresponding change in the borehole pressure P_0 above and beyond the ambient pressure. A fractional change in the phase velocity at a given frequency is expressed as

$$\frac{V^{\text{Stoneley}} - V_{\text{ref}}^{\text{Stoneley}}}{V_{\text{ref}}^{\text{Stoneley}}} = \left[C_1 N_1 + C_2 N_2 + \left.\frac{\Delta V}{V\Delta P}\right|_{\text{fluid}} + \left.\frac{\Delta V}{V\Delta P}\right|_{\text{linear}} \right] P_0 \quad (21)$$

where C_1 and C_2 denote lengthy integrals that can be numerically evaluated as a function of frequency in terms of the known Stoneley wave solution in the ambient state. The quantity, $\Delta V/V\Delta P|_{\text{fluid}}$ denotes the contribution of the borehole fluid nonlinearity to the total change in the Stoneley wave velocity. The other quantity, $\Delta V/V\Delta P|_{\text{linear}}$, denotes the contribution of the formation that can be calculated in terms of the known linear elastic constants and Stoneley wave solution in the ambient state. The sensitivity of the normalized nonlinear constants, N_1 and N_2, to the Stoneley dispersion can be expressed in terms of the integrals C_1 and C_2 at various frequencies. Figure 28 shows the frequency sensitivity of coefficients C_1 and C_2 to the fractional changes in the Stoneley wave velocity caused by a unit ($P_0 = 1$ Pa) increase in the borehole pressure.

Sensitivity of the Flexural Dispersion to the Nonlinear Constants

The sensitivity of the same two normalized nonlinear constants N_1 and N_2 to the flexural dispersion caused by an increase in the borehole pressure can be analyzed in a similar manner as described for the Stoneley dispersion. As before, a fractional change in the flexural velocity at a given frequency is expressed in the following form:

$$\frac{V^{\text{flexural}} - V_{\text{ref}}^{\text{flexural}}}{V_{\text{ref}}^{\text{flexural}}} = \left[D_1 N_1 + D_2 N_2 + \left.\frac{\Delta V}{V\Delta P}\right|_{\text{fluid}} + \left.\frac{\Delta V}{V\Delta P}\right|_{\text{linear}} \right] P_0 \quad (22)$$

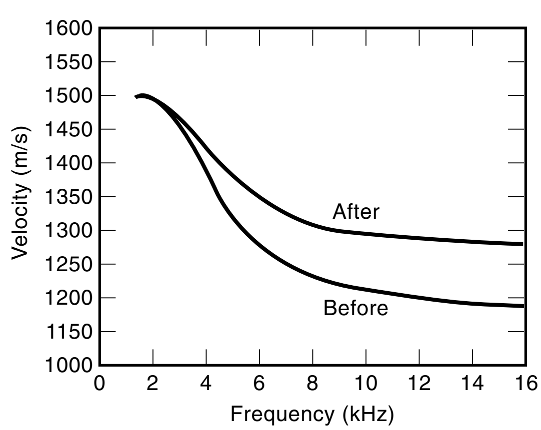

Figure 27. Borehole flexural dispersions before and after an increase in borehole pressure $P_0 = 5$ MPa.

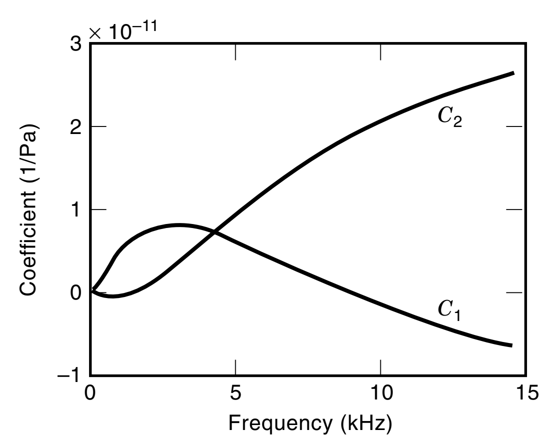

Figure 28. Sensitivity coefficients as a function of frequency for changes in the Stoneley dispersion.

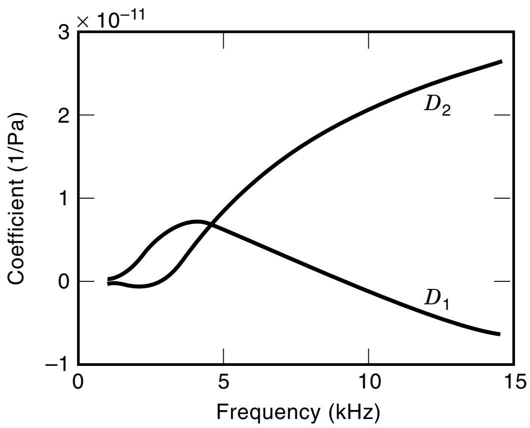

Figure 29. Sensitivity coefficients as a function of frequency for changes in the flexural dispersion.

where D_1 and D_2 denote integrals that can be evaluated as a function of frequency in terms of the known flexural wave solution in the ambient state. Figure 29 displays the frequency sensitivity of coefficients D_1 and D_2 to the fractional changes in the flexural velocity caused by an increase in the borehole pressure of *unit* magnitude (P_0 = 1 Pa). Note that the portions of the fractional changes in the flexural dispersion due to the linear constants of the formation in the ambient state and those due to the nonlinearity of the borehole fluid can also be calculated in terms of the known borehole fluid nonlinearity and the flexural wave solution in the ambient state (36).

Estimation of the Formation Nonlinear Constants

Estimation of the formation nonlinear constants may be carried out from multifrequency inversion of the Stoneley and flexural wave velocity dispersions. The inversion for the formation nonlinear constants may be carried out either from changes in the Stoneley or from flexural dispersions caused by a borehole pressure increase. It may also be carried out by a combination of the Stoneley and flexural dispersion data at more frequencies than the minimum of two that are shown in the illustration given below:

Assuming that fractional changes in the Stoneley velocities at two frequencies f_1 and f_2 are available for a borehole pressure increase of P_0 = 3.447 MPa (500 psi), one can formulate the inversion process in the form of the following equations:

$$\boldsymbol{AX} = \boldsymbol{B} \tag{23}$$

where

$$\boldsymbol{A} = \begin{bmatrix} C_1^{f_1} & C_2^{f_1} \\ C_1^{f_2} & C_2^{f_2} \end{bmatrix} \tag{24}$$

$$\boldsymbol{X} = \begin{bmatrix} N_1 P_0 \\ N_2 P_0 \end{bmatrix} \tag{25}$$

$$\boldsymbol{B} = \begin{bmatrix} \left(\left.\frac{\Delta V}{V}\right|_{\text{Stoneley}} - \left.\frac{\Delta V}{V}\right|_{\text{linear}} - \left.\frac{\Delta V}{V}\right|_{\text{fluid}} \right)_{f_1} \\ \left(\left.\frac{\Delta V}{V}\right|_{\text{Stoneley}} - \left.\frac{\Delta V}{V}\right|_{\text{linear}} - \left.\frac{\Delta V}{V}\right|_{\text{fluid}} \right)_{f_2} \end{bmatrix} \tag{26}$$

Table 2. N_1 and N_2 from Stoneley Dispersions

f (kHz)	$\left.\frac{\Delta V}{V}\right\|_{\text{Stoneley}}$	B	N_1	N_2
1.688	0.0168	0.0149	582	977.5
2.180	0.0219	0.0201	(582)	(979)

where the superscripts and subscripts f_1 and f_2 denote that the quantity is evaluated at those frequencies. The accuracy of the estimates of nonlinear constants are improved if one measures borehole pressure-induced changes in the Stoneley velocities over a frequency band where these constants have larger sensitivity. Table 2 contains the input data of the Stoneley velocity differences at two different frequencies, and the two estimated normalized nonlinear constants of the formation. The actual values of the normalized nonlinear constants N_1 and N_2 are shown in parentheses. Note that the input velocity data are obtained from a forward model. So the only source of error in the estimate is due to the lower sensitivity of the parameter.

As in the case of multifrequency inversion of Stoneley dispersion, one can also employ changes in the flexural dispersions caused by borehole pressurization to estimate the same formation nonlinear constants c_{144} and c_{155} as before. However, note that unlike the Stoneley dispersion, low-frequency flexural dispersion data exhibit negligibly small acoustoelastic effect and are not suitable for estimating the formation nonlinear constants. Nevertheless, estimation of the formation nonlinear constants from the inversion of flexural dispersions in a moderately high frequency band (approximately 3 kHz to 4 kHz) is quite accurate as shown in Table 3.

Estimation of Uniaxial Stress Magnitude

Recently, it has been reported that a flexural dispersion crossover for the fast and slow dipole orientations is an indicator of stress-induced anisotropy dominating over any intrinsic formation anisotropy. Assuming that the azimuthal shear anisotropy is solely due to the difference between the maximum (S_H) and minimum (S_h) stresses in the far-field, the stress difference can be estimated from the following equation:

$$S_H - S_h = \frac{\rho_o (V_{12}^2 - V_{13}^2)}{(1 + c_{456}/c_{66})} \tag{27}$$

where $2c_{456}/c_{66} = N_1 - N_2$; the stresses S_H and S_h are parallel to the X_2 and X_3 directions, respectively; and the borehole is parallel to the X_1 axis. Therefore, estimation of the formation nonlinear constants N_1 and N_2 from sonic measurements while changing borehole pressures allows calculation of the stress difference from the dipole shear anisotropy.

Table 3. N_1 and N_2 from Flexural Dispersions

f (kHz)	$\left.\frac{\Delta V}{V}\right\|_{\text{flexural}}$	B	N_1	N_2
3.412	0.0155	0.0153	582	980
3.995	0.0257	0.0253	(582)	(979)

Estimation of Stress Derivatives of $\rho_0 V_{12}^2$ and $\rho_0 V_{13}^2$

The plane wave velocities for waves propagating along the X_1 direction in an isotropic medium subject to homogeneous biasing normal stresses and strains can be calculated from the equations of motion for small dynamic fields superposed on a bias. Assuming that there is a specimen of the same material as the formation in the ambient state in the form of a rod with the uniaxial stress of magnitude S applied along the rod axis, stress derivatives of shear velocities for waves propagating normal to the rod axis and polarized parallel and normal to the stress direction can be approximated by Eqs. (28) and (29), respectively, as described by Sinha (38):

$$\frac{\rho_0 \partial V_{12}^2}{\partial S} = \frac{(2 - N_2)c_{66}}{Y} + \frac{(N_1 + N_2)\nu c_{66}}{Y} \tag{28}$$

$$\frac{\rho_0 \partial V_{13}^2}{\partial S} = \frac{(\nu N_2 - N_1)c_{66}}{Y} + \frac{(N_2 - 2)\nu c_{66}}{Y} \tag{29}$$

where ν and Y are the formation Poisson's ratio and Young's modulus in the reference ambient state, respectively, and V_{IJ} denotes the plane wave velocity in the reference state for propagation along the X_I direction and polarization along the X_J direction. These stress derivatives are functions of the formation nonlinear constants c_{144} and c_{155} via N_1 and N_2, and linear constants Y and ν refer to the ambient reference state. Substituting the estimated values of the formation nonlinear constants N_1 and N_2 obtained from the inversion of the Stoneley and flexural dispersions before and after borehole pressurization allows calculation of stress derivatives of $\rho_0 V_{12}^2$ and $\rho_0 V_{13}^2$ from Eqs. (28) and (29).

Experimental results by Winkler (39) reveal that a positive slope of $\rho_0 V_{IJ}^2$ generally indicates that the existing stresses in the material are significantly less than the failure stress, whereas a negative slope implies that the existing stresses in the material are substantially close to the failure stress. Agreement is good between the calculated stress derivatives of $\rho_0 V_{12}^2$ and $\rho_0 V_{13}^2$ and those experimentally measured on a specimen of this rock at atmospheric pressure.

In summary, two of the three formation nonlinear constants, c_{144} and c_{155}, can be estimated by inverting changes in the Stoneley and/or flexural dispersions at two different borehole pressures. A sensitivity analysis of these nonlinear constants to the Stoneley and flexural dispersions helps in a proper selection of frequency band for multifrequency inversion of velocities. These two nonlinear constants are sufficient to calculate magnitude of the difference between the maximum and minimum stresses in the azimuthal plane from the dipole shear anisotropy measurements. The same two nonlinear constants are also sufficient to calculate stress derivatives of shear velocities for waves propagating normal to the applied stress in a uniaxially stressed sample of the same material as that of the formation under in situ conditions.

ULTRASONIC MEASUREMENTS

Ultrasonic measurements play an important role in the development and maintenance of an oilfield well. After a well has been drilled, ultrasonic imaging provides the borehole cross-sectional shape and an image of the sedimentary layers, and it detects fractures and faults that intersect the borehole. Geologists use this information to understand the well depositional environment and locate hydrocarbon reservoirs. Well developers use this information to maintain a structurally stable well and optimize productivity of fractured reservoirs. When a well is cased and cemented, ultrasonic measurements help evaluate whether cement has filled the annulus between casing and formation to prevent hydraulic communication between hydrocarbon-bearing and water-bearing zones. Later on, during the well production stage, ultrasonic measurements are used to inspect the integrity of the casing vis-à-vis corrosion.

Ultrasonic waves are used for these applications because they are capable of probing rocks, steel, and cement with millimeter-to-centimeter resolution.

Ultrasonic Pulse-Echo Imaging Technique

Open-hole imaging and casing inspection are based on the pulse-echo technique introduced by Zemanek et al. (40) and improved by Havira (41). In this technique, an ultrasonic piezoelectric transducer in contact with a fluid medium radiates a concentrated acoustic beam of short duration in the direction of the object to be imaged. The beam is reflected at discontinuities where material properties such as density and compressibility change, as is the case at the interface between a fluid and a rock. The amount of reflected acoustic energy depends on the acoustic contrast seen by the beam and on the geometry of the illuminated surface of the object. The same transducer then detects the reflected acoustic energy and converts it into an electric voltage. For maximum signal reception, we direct the transducer beam at normal angle with respect to the plane of the object. As we move the transducer system sidewise and up and down with respect to the object, we record the time of arrival and the amplitude of the reflected signal. We then use this information to determine the location and size of the object and infer some of its acoustic properties. The pulse-echo technique is widely used as a basis for ultrasonic imaging because of its simplicity and effectiveness.

Transducer Assembly and Characteristics

The ultrasonic transducer system used in open- and cased-hole imaging is part of an elaborate assembly called a sonde in the form of a rugged cylindrical tube of 10 cm or less in diameter and tens of meters in length. Figure 30 shows the schematic of an ultrasonic sonde. The sonde houses the transducer(s), an electronics cartridge responsible for signal generation and data acquisition with digital signal processing units, centralizers to help center the sonde during measurement, and, for ultrasonic applications that require it, a motor to rotate the transducer for azimuthal coverage.

The sonde is first lowered into the well. As it is pulled up, continuous ultrasonic measurements are taken and recorded digitally as a function of depth and azimuth. In the case of a rotating transducer system, the transducer scans the formation wall or the casing in a helical path firing every 2°, 5°, 10°, or 20°, depending on the application and resolution required. The data are either stored in memories for subsequent processing at the surface or transmitted to the surface via a wireline. Presently, the data are often processed down hole in real time and then transmitted to the surface for display and

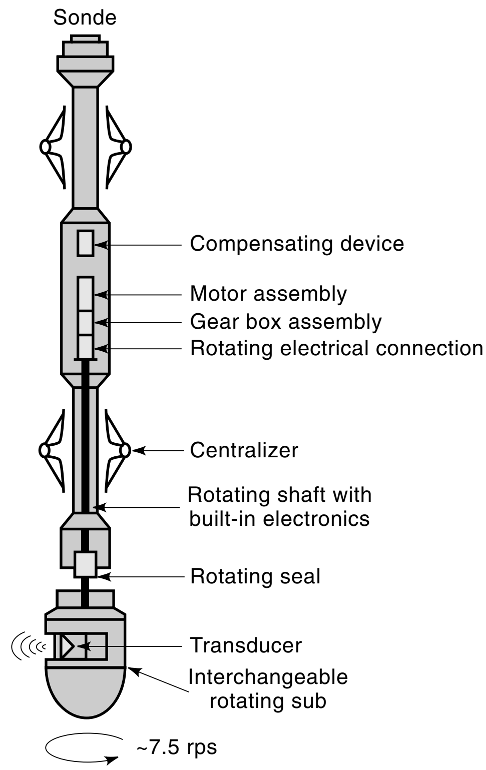

Figure 30. Schematic of an ultrasonic imaging platform which accommodates different transducers and transducer assemblies for the three ultrasonic applications discussed in this article: open-hole imaging, casing inspection, and cement evaluation. The bottom sub, which houses the transducer, rotates at 7.5 rotations per second and fires at various sampling rates depending on the spatial resolution needed. (From Ref. 58.)

printing. The recorded raw and processed data are commonly called logs.

Measurement of the wave speed in the mud is also carried out as it is needed in the data processing. This measurement is carried out either with an additional transducer during the imaging logging or with the same transducer while the tool is lowered into the well. In this latter mode, the transducer is flipped 180° so it faces a built-in target at a known distance. A mud wave speed profile is thus calculated and stored for use in the processing of the data obtained during the logging performed when the tool is pulled up the well.

We use focused apertures, such as spherically curved caps, in open-hole imaging and casing inspection because of the high spatial resolution they provide. This resolution, comparable to the beam size in its focal region, is typically much smaller than the aperture size. The resolution increases with frequency. However, because of the high acoustic attenuation present in the mud, open-hole imaging uses frequencies below a few hundreds of kilohertz. On the other hand, casing corrosion inspection requires higher resolution (of the order of few millimeters) than formation wall imaging and is usually performed at higher frequencies, typically 2 MHz. To ensure that attenuation is not detrimental to the measurement, brine, production fluids, or lighter muds fill the casing during this measurement.

Open-Hole Imaging

Figure 31(a) depicts an ultrasonic pitch-catch imaging of a formation rock in contact with mud. Figure 31(b) shows a time signal generated by the transducer upon detection of the reflected echo. Figure 31(b) also shows the envelope of the time signal which is used to estimate the amplitude and travel time of the reflected echo. The travel time corresponds to the beam propagation in the mud from the transducer aperture to the mud–formation interface and back to the transducer aperture. Let us denote by c_m the acoustic wave speed in the mud and by t_0 the estimated travel time of the reflected echo; then the location, d, of the mud–formation interface with respect to the transducer aperture is given by the simple relation

$$d = c_m t_0/2 \tag{30}$$

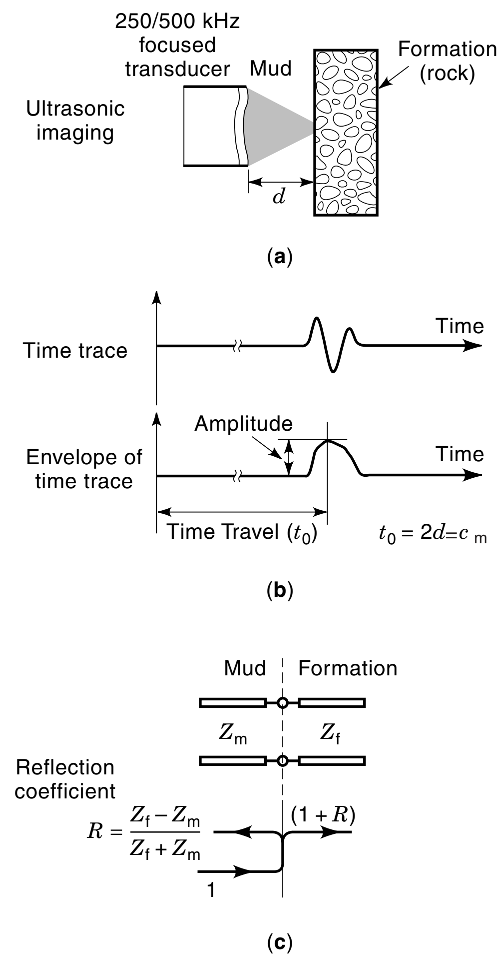

Figure 31. (a) Open-hole ultrasonic imaging. A 250 kHz or 500 kHz-focused transducer beam is used to measure the hole size and image its geological and structural features. (b) A typical transducer time trace features an echo due to reflection from the mud-formation surface. The travel time and amplitude of the envelope peak of the reflected echo are measured and used to estimate the distance to the interface (hence the size of the hole) and detect sedimentary layering, fractures, and faults intersecting the borehole, as well as detect enlargement of the borehole such as breakouts and cavities. (c) A transmission-line analog is used to estimate the acoustic wave reflection coefficient in the pulse-echo technique.

Table 4. Acoustic Parameters for Some of the Layers in a Cased-Hole Environment

Layer	Acoustic Impedance, Z (10^6 kg m^{-2} s^{-1})	Velocity (m/s)	Compressional Density (kg m^{-3})
Water	1.4	1480	1000
Steel	45.86	5880	7800
Cement slurries			
Low-Z cement	3.36	2500	1340
Medium-Z cement	6.51	3375	1930
High-Z cement	8.01	3530	2300
Rock formations			
Shale	4.3–12.0	2133–5181	2016–2316
Sand	6.0–8.2	2743–3505	2187–2340
Limestone	9.43–14.8	3960–5640	2380–2624
Dolomite	20.19	7010	2800

After Nelson (57).

We use d and the known position of the transducer within the hole to calculate the cross-sectional shape of the hole. To estimate the amplitude reflection coefficient of the mud–formation interface due to acoustic contrast, we use an electric transmission-line analogue and the concept of acoustic impedance. To the mud and formation, we assign, respectively, the acoustic impedances $Z_{\mathrm{m}} = \rho_{\mathrm{m}}c_{\mathrm{m}}$ and $Z_{\mathrm{f}} = \rho_{\mathrm{f}}c_{\mathrm{f}}$, where ρ_{m} is the mud density, ρ_{f} is the formation density, and c_{f} is the formation compressional wave speed. Figure 31(c) shows a schematic of the transmission-line analog. Similarly to the voltage reflection coefficient at the junction of two lines in the transmission-line model, we write the acoustic reflection coefficient at the mud–formation interface as

$$R = \frac{Z_f - Z_m}{Z_f + Z_m} \tag{31}$$

Thus a hard rock, which has larger density and compressional wave speed, reflects more acoustic energy than a soft rock. Table 4 lists acoustic properties of some of the layers present in a cased-hole environment. However, because acoustic beam reflection also depends on the roughness and alignment of the surface illuminated by the incident beam, Eq. (31) does not describe the total reflection coefficient at the mud–formation interface. Surface roughness and sharp geometrical discontinuities, such as the boundary of a cavity or a fault intersecting the borehole, scatter acoustic energy over a larger angular range, whereas inclined surfaces with respect to the incident beam deflect energy away from the transducer collecting aperture. Both situations, often encountered in open-hole imaging, result in a decrease of the reflected signal amplitude.

To view and identify the various borehole deformation features, we display colored images of the radius and amplitude. A host of processing algorithms have been developed to automatically or interactively detect and quantitatively characterize borehole deformations such as breakouts, fractures, faults intersecting the borehole, and sedimentary bedding as reported by Barton et al. (42). Figure 32 shows examples of signal amplitude images which exhibit the presence of breakouts and fractures. [Other examples can be found in Hayman et al. (43)].

Applications of Open-Hole Imaging

Open-hole images of breakouts and fractures intersecting the borehole have enabled geophysicists and geologists to determine the stress state and fracture distribution orientation in the surrounding rock. This information in turn enables well developers to maintain a structurally stable well and optimize productivity of fractured reservoirs (44). For instance, breakout orientation and their azimuthal widths as a function of the depth of a vertical well are used to determine the direction of the minimum horizontal stress and help constrain the rock in-situ stress magnitudes as described by Barton et al. (45). Information from the ultrasonic images is used in conjunction with other measurements. In particular, with that from sonic dipole shear anisotropy logging to determine aligned fractures in hard formations as discussed in the section on sonic measurements.

Other borehole deformations include shearing of the borehole along existing fractures and bedding planes, reaming and erosion by pipes which occur during the drilling process, and other irregular hole shapes.

Casing Inspection

Figure 33(a) depicts the mode of operation for casing inspection. Here, the high-frequency (of the order of 2 MHz) transducer beam probes a layered mud–casing–cement structure. The detected signal features two echoes due to reflections at the internal and external walls of the casing. The signal may contain additional later-arriving, but with lesser amplitude, echoes due to reverberation in the casing. Figure 33(b) shows a typical transducer signal and its corresponding envelope. For processing, we estimate and record the travel times and amplitudes of both echoes. The travel time of the first-arriving echo, t_0, yields, as per Eq. (30), the internal radius of the casing. The delay, δt, between the first-arriving and second-arriving echoes allows for computation of the casing thickness, h, from

$$h = c_s\,\delta t/2 \tag{32}$$

where c_s is the compressional wave speed in steel which we assume to be known. Images of the reflection echoes combined with the estimated internal radius and casing thickness provide the means to detect and quantify various features on the casing such as casing damage, holes, metal loss, and pits. Figure 34 shows an example of a three-dimensional display of a severely corroded casing. [Other examples can be found in Hayman et al. (46).]

A typical 2 MHz transducer for casing corrosion has a diameter of 12.7 mm (0.5 in.) and a focal length of 50.8 mm (2.0 in.).

Cement Evaluation: Principle of Operation

Cement evaluation refers to the process of detecting whether cement fills the annulus between casing and formation and inferring the cement compressive strength. Ultrasonic cement evaluation evolved from the need to overcome the limitations of a lower-frequency (20 kHz) sonic measurement which had been used originally for the same purpose. The sonic measurement, carried out monopole source, lacks the azimuthal resolution to pinpoint where, for instance, a mud or gas channel in the cement column is located. The measurement also

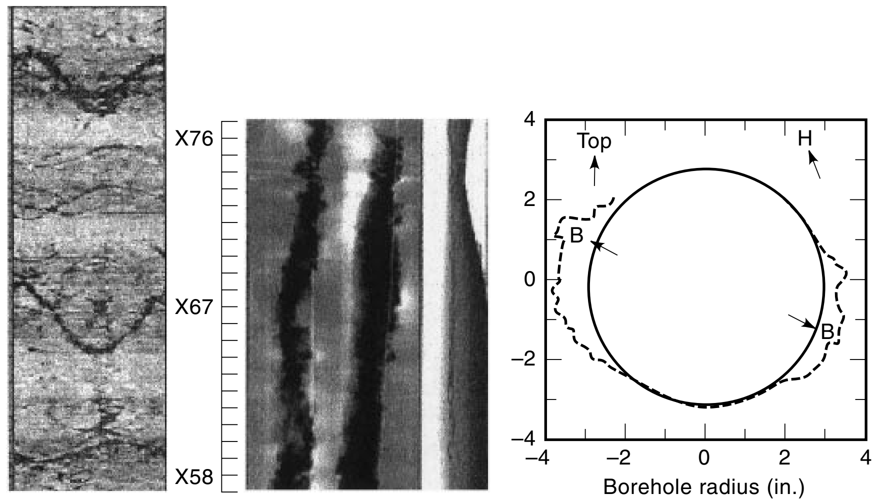

Figure 32. Open-hole ultrasonic imaging in sand/shale environment. Examples of amplitude images versus depth (vertical scale) and azimuth (horizontal scale); dark corresponds to low-amplitude signal. Left image indicates in dark features the presence of fractures intersecting the borehole at various dip (i.e., inclination) angles and alternation of horizontal sand beds, appearing faintly dark, and shale beds, appearing light. Right image indicates in dark the effects of radius enlargements on the signal amplitude. The borehole radius at a fixed depth, obtained from the travel time, is plotted in a dashed line to the right of the image. A circle is also plotted as a reference to highlight deviations from a circular cross section. These radius enlargements, referred to as breakouts, occur diametrically opposed to each other and are induced by nonuniform azimuthal stress concentration around the borehole. (After Ref. 58.)

fails in the case where the cement is not tightly bonded to the casing. This situation can arise from contraction and expansion of the steel casing due to thermal and pressure changes.

Havira (47) introduced the ultrasonic pulse-echo measurement commonly used nowadays for cement evaluation. The measurement technique is based on the excitation of a thickness resonance of the casing. Figure 35 depicts a schematic of this measurement and shows a typical signal which consists of a large head echo due to reflection at the mud–casing interface and a decaying resonance which arises from energy reverberation in the casing. The measurement is based on monitoring the decay of this resonance and relating it to the cement impedance. The cement impedance is then used to infer the cement compressive strength using charts that relate the two parameters. The resonance decays faster when good cement rather than poor (i.e., damaged or contaminated) cement or mud fills the annulus.

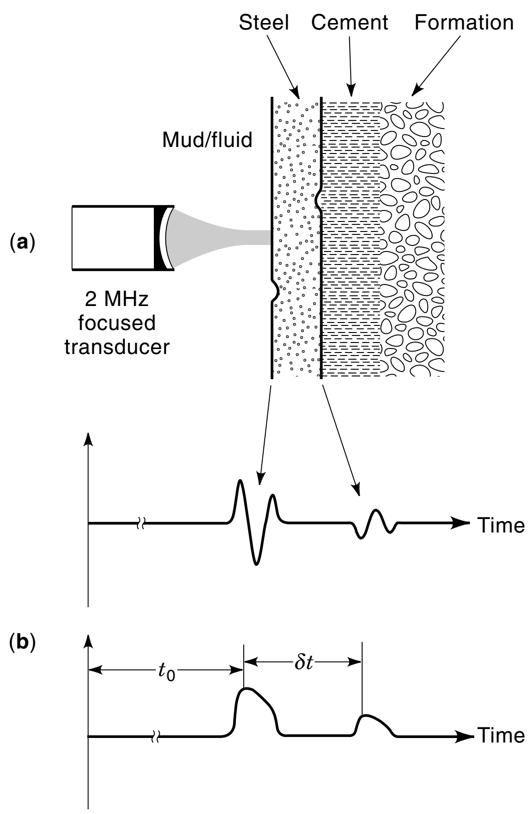

Figure 33. Casing corrosion imaging. A 2 MHz, small-sized (12.7 mm diameter), focused transducer beam is used to image corrosion on the internal and external walls of the casing. The travel time and amplitude of the envelope peaks due to reflections at the inner and outer wall echoes are estimated and used to measure the casing inner radius and thickness. (After Ref. 58.)

The fundamental casing resonance excited at normal incidence corresponds to a frequency, f_0, at which the operating wavelength becomes equal to twice the casing thickness, h,

$$f_0 = \frac{c_s}{2h} \tag{33}$$

To cover the range of thickness of most oilfield casings, generally from 4.5 mm to 15 mm, the transducer bandwidth is selected to be of the order of a few hundred kilohertz, corresponding to the range between 190 kHz and 650 kHz. The transducer aperture is optimized for maximum excitation of the casing fundamental thickness mode; the aperture radiates a pulsed beam whose wavefront nearly conforms with the internal concave wall of the casing. This particular thickness mode is known to be the first high-order symmetric Lamb mode, S_1, as noted by Randall and Stanke (48).

Cement Evaluation: Processing

To quantify the decay rate of the casing resonance and thus determine the acoustic impedance of the annulus medium, various approaches have been used. The existing approaches, which are typically constrained by the requirement to be implentable downhole, evolved from simple schemes to elaborated methods. This evolution has been enabled by the advent of more powerful electronic technology capable of handling high-temperature and high-pressure environments. Havira (47) initially used waveform windowing by taking the ratio of the acoustic energy present in the decaying part of the waveform to that of the head echo such that mud attenuation and beam diffraction in the fluid are taken into account. The ratio is then calibrated to that of a free pipe condition, where fluid fills the annulus, and expressed as an impedance of the

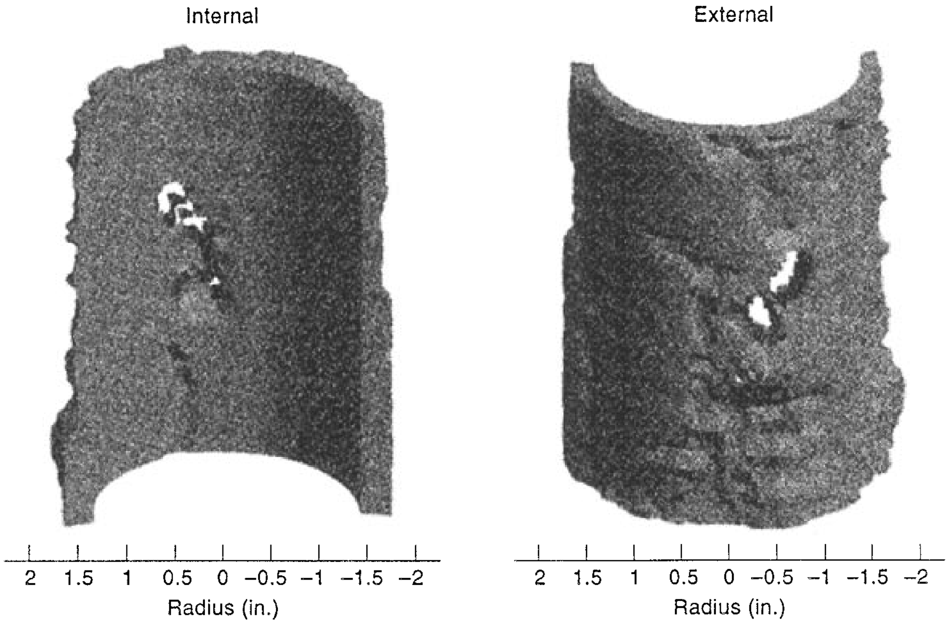

Figure 34. Casing corrosion imaging. Three-dimensional amplitude images show the severe exterior corrosion in the outside of the casing wall and holes on the inside wall. The images shown are for half of the casing. (After Ref. 58.)

annulus. Kimball (49) further improved this method by narrow-band filtering to capture the contribution of the fundamental casing mode and exclude that due to higher-order modes.

Hayman et al. (50) recently introduced a processing method which uses a plane-wave model to iteratively fit the measured signal. The model makes use of known values for the steel impedance and wave speed and of the measured value of the mud impedance. It then uses the casing thickness and cement impedance as free parameters to adjust for the fit. For this purpose, both model-generated and measured signals are first preprocessed to extract the casing thickness and a measure of the cement impedance. This is done by calculating the group delay (the derivative of the phase with respect to frequency) of the signal which is nearly flat except at the resonances which produce minima. The frequency, f_0, of the fundamental mode minimum is used to calculate the casing thickness as per Eq. (33), whereas its width, Δf, is used as a measure of the cement impedance. The iterative scheme stops when f_0 and Δf from the measured and model-generated signals match within some chosen error criterion. To correct for the nonplanar geometry of the plane-wave model, Randall and Stanke (48) developed a 3-D cylindrical model for this measurement and provided correction tables.

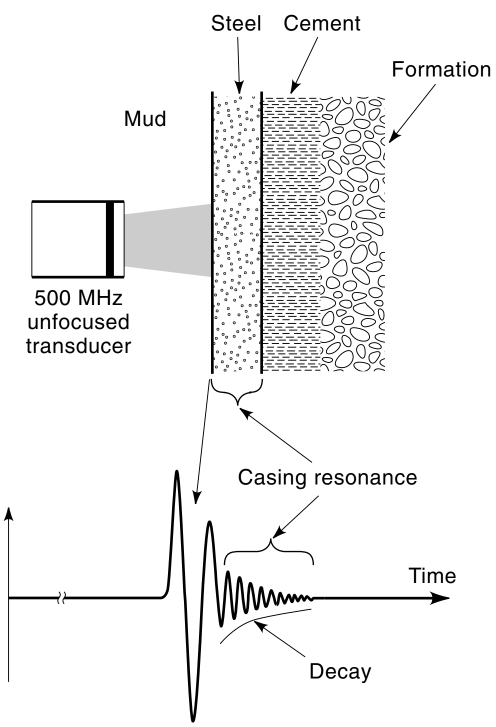

Figure 35. Cased-hole cement evaluation. A 500 kHz unfocused transducer beam is used to excite a strong casing thickness resonance whose amplitude decay depends on whether cement is present behind the casing or not. The amplitude and travel time of the first echo due to the mud–casing interface is monitored for low-resolution casing inspection.

Cement Evaluation: A Plane-Wave Model

The following intuitively simple model helps to predict and interpret the signal generated in this thickness resonance measurement. We assume that the transducer emits plane waves which interact at normal incidence with a seismic-like plane-layered mud–casing–cement structure as shown in Fig. 35. Figure 36 depicts the transmission-line analog which we use to formulate the total reflection coefficient, $R(\omega)$, for an incident plane wave with unit amplitude and angular frequency ω. Upon reflection and transmission at each interface, the plane-wave amplitude is multiplied by the interface reflection and transmission coefficients, respectively. As it propagates in the casing layer from one interface to the other, the plane wave acquires a phase accumulation equal to $\exp\{jk_s h\}$, where $k_s = \omega/c_s$ is the compressional wavenumber in steel. Following these rules and using $T = 2h/c_s$, we write $R(\omega)$ in the sequence

$$R(\omega) = R_1 + (1+R_1)[1 + (-R_2R_1e^{j\omega T}) + (-R_2R_1e^{j\omega T})^2 + \cdots]R_2(1-R_1)e^{j\omega T} \tag{34}$$

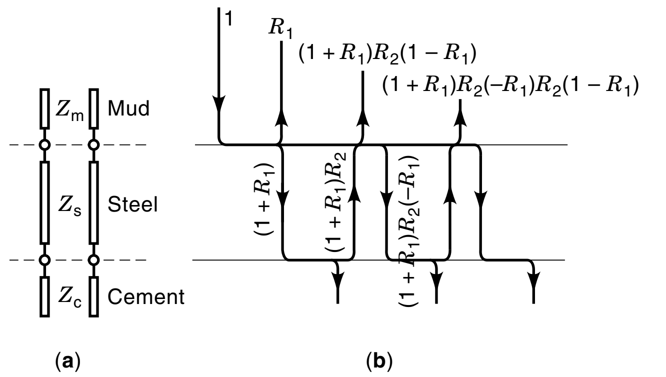

Figure 36. (a) Transmission-line analog to the layered mud–steel–cement configuration with associated acoustic impedances. (b) The plane-wave reflection coefficient from the layered configuration is derived by considering multiple reflections within the steel layer. The sketch shows the first three reflections and their amplitudes in the mud.

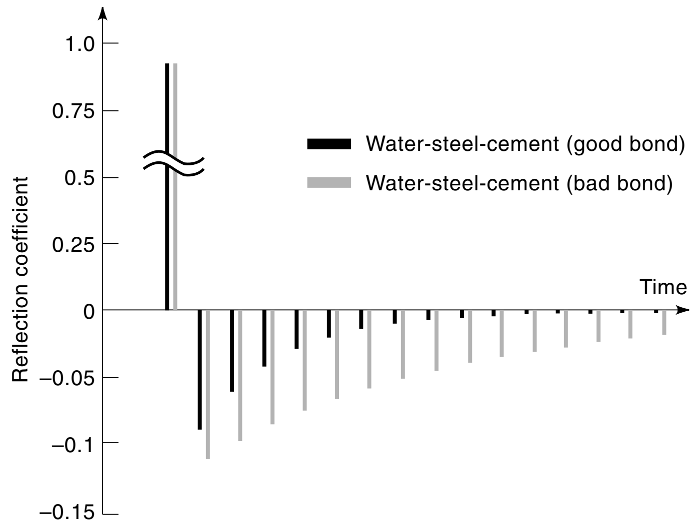

Figure 37. Pulse-echo impulse response from the layered mud–steel–cement configuration shown in Fig. 36. Note that the positive and negative parts of the vertical scale are dissimilar to accommodate the strong reflection from the mud–steel interface.

which can be written in closed form as Havira (47) noted:

$$R(\omega) = R_1^{-1} + \frac{R_1 - R_1^{-1}}{1 + R_1 R_2 e^{j\omega T}} \tag{35}$$

Here, R_1 and R_2 are the acoustic reflection coefficients at the mud–casing and casing–cement interfaces, respectively. According to Eq. (31), R_1 and R_2 are given in terms of the acoustic impedances of the mud layer (Z_m), the steel layer (Z_s), and cement layer (Z_c):

$$R_1 = \frac{Z_s - Z_m}{Z_s + Z_m}, \quad R_2 = \frac{Z_c - Z_s}{Z_c + Z_s} \tag{36}$$

where δ is the Dirac delta function. We obtain the impulse response of the transducer within this model by Fourier transform of $R(\omega)$ in Eq. (35):

$$\begin{aligned} r(t) &= \int R(\omega) e^{-j\omega t}\, d\omega \\ &= R_1 \delta(t) + (R_1 - R_1^{-1}) \sum_{n=1}^{\infty} |R_1 R_2|^n \delta(t - nT) \end{aligned} \tag{37}$$

We plot this time sequence in Fig. 37 for two cases. The first case corresponds to water–steel–water with $R_1 = -R_2 = 0.937$. The second case corresponds to water–steel–cement with $R_2 = -0.731$. In interpreting these data, we refer to the former case as bad bond (no cement) and refer to the latter case as good bond (to mean that the cement is in contact with the casing).

Cement Evaluation: A Three-Dimensional Rigorous Model

Optimization of the pulse-echo measurement and development of accurate and robust signal processing methods require the use of a more rigorous model than the plane-wave model presented above. A three-dimensional rigorous theory needs to account for the radiation and reception characteristics of the transducer, the beam propagation in the fluid, and the beam interaction with the cylindrically layered fluid–steel–cement–formation structure as schematized in Fig. 38. If one assumes a canonical configuration where all layers are concentric, these requirements can be conveniently taken into account in the frequency domain by expressing the transducer voltage via a two-dimensional spectral wavenumber integral. This integral results from decomposition of all pertinent wave fields in terms of plane waves along the cylindrical axis, z, with a continuous wavenumber β corresponding to z, and angularly propagating waves along the azimuthal direction, ϕ, indexed with a continuous wavenumber ν corresponding to the azimuthal variable ϕ; interested readers may refer to Ref. 51 and 52. The time-domain voltage, $e(t)$, is then recovered from a fast Fourier transform (FFT) of the frequency-domain

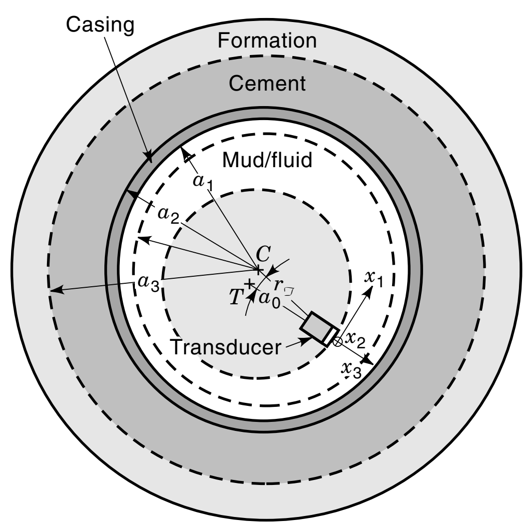

Figure 38. Geometry of the configuration considered in the three-dimensional rigorous model for cement evaluation. A transducer supported by a tool insonifies in pulse-echo mode a cylindrically layered mud–casing–cement–formation medium. The configuration extends out of the plane of the paper along the casing axis. a_0, radius of tool; $r_{\mathcal{T}}$, radius of transducer aperture center; r_0, intermediary fictitious surface used in the analysis.

data based on

$$e(t) = \int E(\omega)e^{-j\omega t}\,d\omega \tag{38}$$

where $E(\omega)$ is the frequency-domain voltage given by

$$E(\omega) = \frac{\gamma(\omega)}{\pi^3\omega\rho_m}\iint_{-\infty}^{\infty}\hat{p}(r_0;\nu,\beta)\hat{p}(r_0;-\nu,-\beta)\Gamma(\nu,\beta)\frac{H_\nu^{(1)}(\kappa_m a_1)}{H_\nu^{(2)}(\kappa_m a_1)} \times [H_\nu^{(1)}(\kappa_m r_0)]^{-2}\,d\nu\,d\beta \tag{39}$$

with

$$\kappa_m = \sqrt{k_m^2 - \beta^2}, \quad k_m = \omega/c_m \tag{40}$$

In this formulae, the outgoing ($H_\nu^{(1)}$) and incoming ($H_\nu^{(2)}$) Hankel functions of real order ν account for wave propagation in cylindrical geometry, $\hat{p}(r_0;\ \nu,\ \beta)$ is the spectral amplitude of the pressure wave at $r = r_0$ radiated by the transducer within the $(\nu,\ \beta)$-spectral decomposition; it represents the radiation and reception characteristics of an electroacoustically reciprocal transducer, and $\Gamma(\nu,\ \beta)$ is a spectral reflection coefficient accounting for the interaction of the $(\nu,\ \beta)$ pressure wave component with the cylindrically layered medium with reference to the innermost interface at a_1; we compute $\Gamma(\nu,\ \beta)$ by considering elastic wave propagation and appropriate boundary conditions in the layered medium. Finally, the frequency-dependent quantity $\gamma(\omega)$ accounts for the temporal spectrum of the transmitter and receiver electronics; it is typically derived from an appropriate calibration experiment.

We assume that the transducer-sensitive aperture of surface A and known normal velocity distribution v_n can be considered to be surrounded by an infinite rigid baffle. Accordingly, we can use the well-known Rayleigh–Sommerfeld formula to compute the pressure $p(r_0,\ \phi,\ z)$ radiated at a cylindrical surface of radius r_0,

$$p[\boldsymbol{x} \equiv (r_0,\phi,z)] = -2j\omega\rho_m \iint_{A_T} G_f(\boldsymbol{x};\boldsymbol{x}')v_n(\boldsymbol{x}')\,dA \tag{41}$$

where $dA \equiv dx_1dx_2$ is an element of integration over A and $G_f(\boldsymbol{x};\boldsymbol{x}')$ is the three-dimensional "free-field" Green's function,

$$G_f(\boldsymbol{x};\boldsymbol{x}') = \frac{e^{jk_f|\boldsymbol{x}-\boldsymbol{x}'|}}{4\pi|\boldsymbol{x}-\boldsymbol{x}'|} \tag{42}$$

The two-dimensional Fourier transform then yields $\hat{p}(r_0;\ \nu,\ \beta)$ as

$$\hat{p}(r_0;\nu,\beta) = \int d\phi \int dz\,p(r_0,\phi,z)\exp\{-j[\nu\phi + \beta z]\} \tag{43}$$

The integrals are carried out numerically over domains of integration $\mathcal{D}_\phi$ along ϕ and $\mathcal{D}_z$ along z over which $p(r_0,\ \phi,\ z)$ is not vanishingly small.

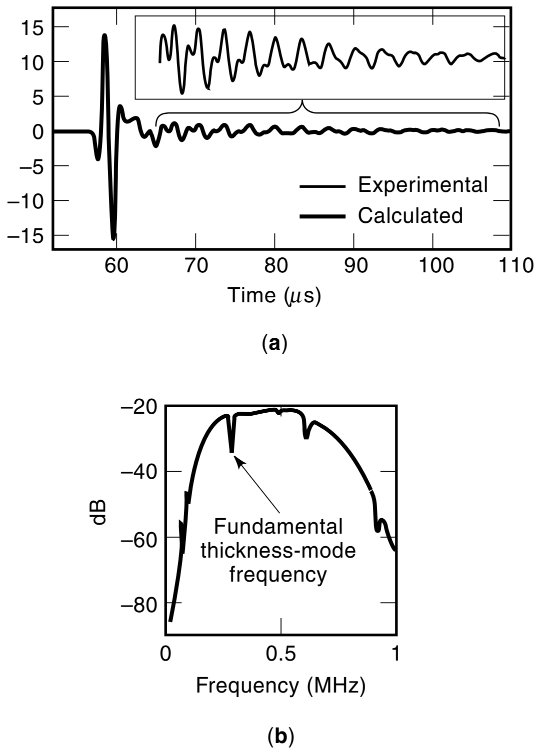

Figure 39. (a) Comparison between experimental (dark solid) transducer signal and calculated signal (light solid) from the three-dimensional rigorous model for the cement evaluation pulse-echo measurement for a steel pipe loaded with water on both sides. (b) Comparison between associated Fourier spectral amplitudes. The inset in (a) shows an expanded view of the casing resonant response. The notch in the spectral amplitude profile in (b) around 0.3 MHz indicates the fundamental casing thickness resonance which is at the basis of the measurement; its position and spectral width are related to the casing thickness and the impedance of the medium in the annulus in contact with the casing.

Figure 39 displays an example of computed and experimental signals for a 9.5 mm thick casing with water filling the inside and outside of the casing. The transducer has a 10 mm by 30 mm rectangular aperture with a nearly uniform v_n and is positioned at 42 mm from the casing internal wall. The model-calculated signal in Fig. 39(a) and its Fourier spectrum in Fig. 39(b), both shown in gray, agree very well with the experimental signal and its spectrum shown in dark solid. The inset in Fig. 39(a) shows an expanded view of the casing resonant response. Figure 40 displays a similar comparison, but for the case of a cemented casing with water as formation. The cement thickness is 38 mm. The inset plot in Fig. 40 shows the extracted contribution due to reflection at the cement–water interface. We compute this contribution by subtracting the signal pertaining to the 38 mm thick cement from the signal pertaining to a significantly thicker cement under the same conditions. To capture $\gamma(\omega)$ needed in Eq. (39), an independent calibration experiment involving reflection from a very thick casing is performed. (Interested readers may refer to Ref. 52.)

Recent Developments in Ultrasonic Measurements

Recent developments have focused on (1) enhancing open-hole imaging and cement evaluation methods with advanced sig-

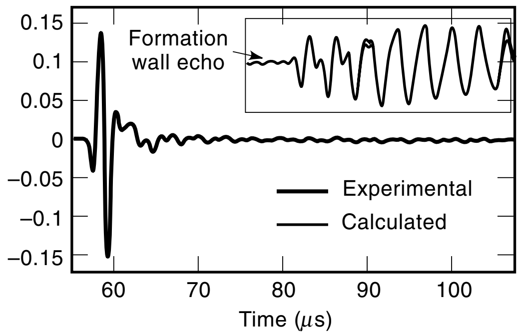

Figure 40. Comparison between calculated (light solid) and experimental (dark solid) waveform for a pulse-echo measurement from a steel pipe cemented on the outside. The inset shows an expanded view of the extracted echo due to reflection from the end of the 38.1 mm thick cement. The extraction of this echo is done by subtracting the signal from a similar one corresponding to the same conditions except that the cement is significantly thicker.

nal processing methods and novel transducer design and (2) identifying new applications of ultrasonic measurements. Current cement evaluation techniques have limitations to address, for instance, lightweight and flexible cements. These latter are used because of their optimized mechanical properties to certain well conditions. Lightweight and flexible cements have acoustic properties that are similar to that of mud and thus pose big challenges to the current tools (53).

Miller and Stanke (54) proposed a signal processing method to augment the applications of present cement evaluation pulse-echo techniques to deeper radial imaging (up to the formation wall). Their method extracts the echoes arising from reflection at the cement-formation interface from data acquired with commercial tools. The method uses a series of steps that suppress the early-arriving large echo in the signal and diminish the casing resonance to a level at which the cement-formation interface echoes, when they are present in the original data, become detectable. Miller and Stanke have shown that their method is effective whenever there is indication from the estimated cement impedance that the casing resonance is effected by reflections from the cement-formation interface (54). Rao et al. (55) have proposed an ultrasonic system with a separate transmitter and receiver aligned with the casing axis so as to propagate acoustic energy in the casing. The amplitude decay of the propagatory signal, measured at two receivers, shows clear correlation with the cement properties.

Ultrasonic measurements are now used in conjunction with formation evaluation measurements conducted during the drilling process; these measurements are referred to as logging while drilling. Moake et al. (56) recently introduced a new ultrasonic system with three transducers operating in pulse-echo mode to provide the shape of the hole. This information is used by other measurements (e.g., nuclear) to compensate for the presence of mud in the inversion for formation properties.

The areas of cement evaluation and annulus and formation wall imaging in cased wells is the subject of renewed interest nowadays and would probably remain so in the foreseeable future. This interest in developing enhanced and more reliable ultrasonic measurements parallels that in the oil field business to reevaluate the potential and optimize the productivity of existing cased wells.

ACKNOWLEDGMENTS

The authors acknowledge permission from Schlumberger Educational Services to include published materials (in Figs. 1, 3–9, 16, 17, 30, 32, 34), and they are grateful to John Ullo of Schlumberger–Doll Research for his support and careful reading of the manuscript.

BIBLIOGRAPHY

1. D. V. Ellis, *Well Logging for Earth Scientists,* Amsterdam, The Netherlands: Elsevier, 1987, Chaps. 15–17.
2. J. Tittman, *Geophysical Well Logging,* New York: Academic Press, 1986.
3. M. R. J. Wyllie, A. R. Gregory, and L. W. Gardner, Elastic wave velocities in heterogeneous and porous media, *Geophysics,* **21**: 41–70, 1956.
4. F. L. Paillet and J. E. White, Acoustic modes of propagation in the borehole and their relationship to rock properties, *Geophysics,* **47**: 1215–1228, 1982.
5. F. L. Paillet and C. H. Cheng, A numerical investigation of head waves and leaky modes in fluid-filled boreholes, *Geophysics,* **51**: 1438–1449, 1986.
6. B. E. Hornby, Tomographic reconstruction of near-borehole slowness using refracted boreole sonic arrivals, *Geophysics,* **58**: 1726–1738, 1993.
7. D. M. Williams, The acoustic log hydrocarbon indicator, *SPWLA 31st Annu. Logging Symp.,* 1990.
8. C. V. Kimball and T. M. Marzetta, Semblance processing of borehole acoustic array data, *Geophysics,* **49**: 264–281, 1984.
9. B. E. Hornby et al., Fracture evaluation using reflected Stoneley wave arrivals, *Geophysics,* **54** (10): 1274–1288, 1989.
10. K. W. Winkler, H. L. Liu, and D. L. Johnson, Permeability and borehole Stoneley waves: Comparison between experiment and theory, *Geophysics,* **54**: 66–75, 1989.
11. X. M. Tang and C. H. Cheng, Borehole Stoneley wave propagation across permeable structures, *Geophys. Prospecting,* **41**: 165–187, 1993.
12. F. L. Paillet and C. H. Cheng, *Acoustic Waves in Boreholes,* Boca Raton, FL: CRC Press, 1991.
13. J. L. Stevens and S. M. Day, Shear velocity logging in slow formations using the Stoneley waves, *Geophysics,* **51**: 137–147, 1986.
14. C. H. Cheng, M. N. Toksoz, and M. E. Willis, Determination of in-situ attenuation from full waveform acoustic logs, *J. Geophys. Res.,* **87**: 5477–5484, 1982.
15. J. E. White, *Underground Sound: Application of Seismic Waves,* Amsterdam, The Netherlands: Elsevier, 1983.
16. A. L. Kurkjian and S. K. Chang, Acoustic multipole sources in fluid-filled boreholes, *Geophysics,* **51**: 148–163, 1986.
17. D. P. Schmitt, Shear wave logging in elastic formations, *J. Acoust. Soc. Am.,* **84**: 2215–2229, 1988.
18. A. R. Harrison et al., Acquisition and analysis of sonic waveforms from a borehole monopole and dipole source for the determination of compressional and shear speeds and their relation to rock mechanical properties and surface seismic data, paper SPE 20557, *SPE Annu. Tech. Conf. and Exhibition, New Orleans,* 1990.
19. B. K. Sinha, Sensitivity and inversion of borehole flexural dispersions for formation parameters, *Geophys. J. Int.,* **128** (1): 84–96, 1997.

20. C. V. Kimball, Shear slowness measurement by dispersive processing of the borehole flexural mode, *Geophysics,* **63**: 337–344, 1998.
21. M. P. Ekstrom, Dispersion estimation from borehole acoustic arrays using a modified matrix pencil algorithm, paper presented at the *29th Asilomar Conf. Signals Syst. Comput.,* Pacific Grove, CA, October 31, 1995.
22. R. Burridge and B. K. Sinha, Inversion for formation shear modulus and radial depth of investigation using borehole flexural waves, *66th Annu. Int. SEG Meet.,* Expanded Abstracts, 1996, pp. 158–161.
23. L. Thomsen, Weak elastic anisotropy, *Geophysics,* **51**: 1954–1966, 1986.
24. A. N. Norris and B. K. Sinha, Weak elastic anisotropy and the tube wave, *Geophysics,* **58** (8): 1091–1098, 1993.
25. B. A. Auld, *Acoustic Fields and Waves in Solids,* Vols. I and II, New York: Wiley, 1973.
26. K. H. Ellefsen, C. H. Cheng, and M. N. Toksoz, Applications of perturbation theory to acoustic logging, *J. Geophys. Res.,* **96**: 537–549, 1991.
27. B. K. Sinha, A. N. Norris, and S. K. Chang, Borehole flexural modes in anisotropic formations, *Geophysics,* **59**: 1037–1052, 1994.
28. B. K. Sinha and S. Kostek, Stress-induced azimuthal anisotropy in borehole flexural waves, *Geophysics,* **61** (6): 1899–1907, 1996.
29. C. Esmersoy et al., Dipole shear anisotropy logging, *64th Annu. Int. Meet. Soc. Expl. Geophys.,* Expanded Abstracts, 1994, pp. 1139–1142.
30. M. Schoenberg and C. M. Sayers, Seismic anisotropy of fractured rock, *Geophysics,* **60**: 204–211, 1995.
31. H. D. Leslie and C. J. Randall, Multipole sources in deviated boreholes penetrating anisotropic formations: Numerical and experimentals results, *J. Acoust. Soc. Am.,* **91**: 12–27, 1992.
32. R. M. Alford, Shear data in the presence of aximuthal anisotropy, *56th Ann. Int. Meet., Soc. Expl. Geophys.,* Expanded Abstracts, 1986, pp. 476–479.
33. M. Mueller, A. Boyd, and C. Esmersoy, Case studies of the dipole shear anisotropy log, *64th Annu. Int. Meet. Soc. Expl. Geophys.,* Expanded Abstracts, 1994, pp. 1143–1146.
34. B. K. Sinha et al., Stress-induced dipole anisotropy in a dry Berea sandstone, *65th Ann. Int. Meet., Soc. Expl. Geophys.,* Expanded Abstracts, 1995, pp. 22–25.
35. K. W. Winkler, B. K. Sinha, and T. J. Plona, Effects of borehole stress concentrations on dipole anisotropy measurements, *Geophysics,* **62** (1): 11–17, 1998.
36. B. K. Sinha, S. Kostek, and A. N. Norris, Stoneley and flexural modes in pressurized boreholes, *J. Geophys. Res.,* **100** (B11): 22,375–22,381, 1995.
37. S. Kostek, B. K. Sinha, and A. N. Norris, Third-order elastic constants for an inviscid fluid, *J. Acoust. Soc. Am.,* **94**: 3014–3017, 1993.
38. B. K. Sinha, Estimation of formation nonlinear constants by sonic measurements while changing borehole pressures, *66th Annu. Int. SEG Meet.,* Expanded Abstracts, 1996, pp. 118–121.
39. K. W. Winkler, Azimuthal velocity variations caused by borehole stress concentrations, *J. Geophys. Res.,* **101** (B4): 8615–8621, 1996.
40. J. Zemanek et al., The Borehole televiewer—a new concept for fracture location and other types of borehole inspection, *JPT,* **25**: 762–774, 1969.
41. R. M. Havira, Ultrasonic techniques in oil well logging, *Proc. IEEE Ultrason. Symp.,* November 1986, pp. 563–571.
42. C. A. Barton, L. G. Tesler, and M. D. Zoback, Interaction image analysis of borehole televiewer data, in I. Palaz and S. K. Sengupta (eds.), *Automated Pattern Analysis in Petroleum Exploration,* New York: Springer-Verlag, 1992, Chap. 12, pp. 223–248.
43. A. J. Hayman et al., Improved borehole imaging by ultrasonics, paper SPE 28440, 69th SPE *Annu. Tech. Conf. Exhibition,* New Orleans, LA, 1994.
44. F. L. Paillet et al., Borehole imaging and its application in well logging—an overview, in *Borehole Imaging: Society of Professional Well Log Analysts Reprint Volume,* Chap. 1, 1990, pp. 1–23.
45. C. A. Barton et al., Utilizing wellbore image data to determine the complete stress tensor: Applications to permeability anisotropy and wellbore stability, *Log Anal.* 21–33, Nov.–Dec. 1997.
46. A. J. Hayman et al., Quantitative corrosion evaluation in wells using a multi-function ultrasonic imager, *Proc. IEEE Ultrason. Symp.,* 1995.
47. R. M. Havira, Ultrasonic cement bond evaluation, *SPWLA 23rd Annu. Logging Symp.,* July, 1982.
48. C. J. Randall and F. E. Stanke, Mathematical model for internal inspection of cylindrically layered structures, *J. Acoust. Soc. Am.,* **83**: 1295–1305, 1988.
49. C. V. Kimball, Improved processing for oil well cement evaluation—A study with theoretical and laboratory data, *IEEE Trans. Ultrason. Ferroelectr. Freq. Control,* **39**: 148–158, 1992.
50. A. J. Hayman, R. Hutin, and P. V. Wright, High-resolution cementation and corrosion imaging by ultrasound, paper presented at the 1991 *SPWLA 32nd Annu. Logging Symp.,* TX, 1991.
51. S. Zeroug, Spectral integral formulae for the response of acoustic transducer in cylindrically-curved configurations, *IEEE Trans. Ultrason., Ferroelectr. Freq. Control,* **45**: 768–778, 1998.
52. S. Zeroug, A forward analytical model for ultrasonic pulse-echo measurements in cased oil wells: Theory and experimental validation, Schlumberger–Doll Research report, 1996.
53. *Cement Sheath Evaluation,* API Technical Report 10TR1, American Petroleum Institute, June 1996.
54. D. Miller and F. E. Stanke, Method of analyzing waveforms, US Pat. Appli. Serial No 08/609,114, Filed: Feb. 29, 1996. Allowed-Patent pending.
55. R. Rao et al., Parametric study of cement bond evaluation using early refracted arrivals, *SPWLA 38th Annu. Logging Symp.* 1997.
56. G. L. Moake et al., Standoff and caliper measurements while drilling using a new formation-evaluation tool with three ultrasonic transducers, *SPE Drill. Completion,* **June**: 104–111, 1995.
57. E. B. Nelson, *Well Cementing,* Ridgefield, CT: Dowell Schlumberger, Schlumberger Educational Services, 1990, Sec. 16-4.
58. Schlumberger, 1993.

Bikash K. Sinha
Smaine Zeroug
Schlumberger–Doll Research